JMB

Optimal Determination of Particle Orientation, Absolute Hand, and Contrast Loss in Single-particle Electron Cryomicroscopy

Peter B. Rosenthal* and Richard Henderson

MRC Laboratory of Molecular Biology, Hills Road, Cambridge CB2 2QH, UK

A computational procedure is described for assigning the absolute hand of the structure of a protein or assembly determined by single-particle electron microscopy. The procedure requires a pair of micrographs of the same particle field recorded at two tilt angles of a single tilt-axis specimen holder together with the three-dimensional map whose hand is being determined. For orientations determined from particles on one micrograph using the map, the agreement (average phase residual) between particle images on the second micrograph and map projections is determined for all possible choices of tilt angle and axis. Whether the agreement is better at the known tilt angle and axis of the microscope or its inverse indicates whether the map is of correct or incorrect hand. An increased discrimination of correct from incorrect hand (free hand difference), as well as accurate identification of the known values for the tilt angle and axis, can be used as targets for rapidly optimizing the search or refinement procedures used to determine particle orientations. Optimized refinement reduces the tendency for the model to match noise in a single image, thus improving the accuracy of the orientation determination and therefore the quality of the resulting map. The hand determination and refinement optimization procedure is applied to image pairs of the dihydrolipoyl acetyltransferase (E2) catalytic core of the pyruvate dehydrogenase complex from *Bacillus stearothermophilus* taken by low-dose electron cryomicroscopy. Structure factor amplitudes of a three-dimensional map of the E2 catalytic core obtained by averaging untilted images of 3667 icosahedral particles are compared to a scattering reference using a Guinier plot. A noise-dependent structure factor weight is derived and used in conjunction with a temperature factor ($B = -1000$ Å^2) to restore high-resolution contrast without amplifying noise and to visualize molecular features to 8.7 Å resolution, according to a new objective criterion for resolution assessment proposed here.

© 2003 Elsevier Ltd. All rights reserved.

Keywords: electron cryomicroscopy; single particle reconstruction; absolute hand; pyruvate dehydrogenase; tilt pairs

*Corresponding author

Introduction

Electron cryomicroscopy can be used to determine the structure of unstained proteins and macromolecular assemblies in rapidly frozen thin films of amorphous ice without the need for

Abbreviations used: CTF, contrast transfer function; MTF, modulation transfer function.

E-mail address of the corresponding author: rose@mrc-lmb.cam.ac.uk

crystals. For thin specimens, particle images in electron micrographs after correction for the phase contrast transfer function (CTF) are projections of the structure, and three-dimensional maps of the structure can be calculated by recording all the unique projections required to a given resolution. Different projections can be obtained by tilting the specimen as in electron tomography. However, radiation damage prevents the recording of even a single image with high signal-to-noise ratio from an unstained protein molecule in ice, and it is

necessary to align and average noisy, low-contrast images of many particles in many orientations recorded under low-dose conditions ($5-20\,e^-/\text{Å}^2$). A theoretical estimate suggests that averaging less than 10^6 images may in principle be sufficient to determine the structure of a protein to atomic resolution, provided the position and orientation of the particles can be determined from low-contrast images.[1] Improvements in the quality of images as well as in the computational procedures for determining structures from images are required to realize this in practice.

Methods have been described for calculating low-resolution maps *de novo* from untilted projection data by classifying and averaging similar images and then determining the relative orientation of the average projections in three dimensions, termed angular reconstitution.[2] Iterative model-based refinement, which compares the agreement between projections of the model and the experimental images, can then be used to improve the assignment of single-particle orientations and microscope parameters leading to better and higher-resolution models. Because images of proteins in ice have low contrast, noise can lead to incorrect determination of particle orientations. The difficulty in assessing whether a model has aligned to signal or noise leads to a danger of model bias.[3]

Untilted projection data alone cannot determine absolute hand, since exactly the same views can be produced by a three-dimensional model of the opposite hand. Thus, knowledge of the absolute orientation of two views of the particle is required, otherwise the arbitrary hand of a starting model will persist during refinement. If a map is at high enough resolution, the recognition of individual molecular features or interpretation with a high-resolution X-ray model of a component can indicate which hand is correct. Klug & Finch[4-7] first described tilting experiments for the determination of the absolute hand of negatively stained icosahedral viruses, and more recently a computational procedure for hand determination has been described.[8]

In this study, we describe an extension of these hand determination procedures which is straightforward to perform and can be used as a tool to optimize the determination of particle orientations and to improve the fidelity of the resulting structure determination. The computational procedure depends on comparison of particle orientations on micrographs recorded from tilted and untilted specimens. We apply it to high-resolution, low-dose images of the dihydrolipoyl acetyltransferase (E2) catalytic core of the pyruvate dehydrogenase complex of *Bacillus stearothermophilus*. We then examine the factors that influence the determination of particle orientations and which therefore affect the confidence with which correct hand can be discriminated from incorrect hand. We show that the known tilt angle and tilt axis in the experiment can be used as unbiased targets for rapidly

optimizing the computational parameters that influence the accuracy of orientation determination. Using these optimized parameters leads to better particle orientations and to better three-dimensional maps from untilted data.

In order to visualize the highest-resolution features once such a map is obtained, it is necessary to correct for the loss of contrast in the map at high resolution from causes such as radiation damage, imaging imperfections, and errors in the reconstruction procedure. We estimate the decay in the structure factor amplitudes with resolution by comparing structure factors on an absolute scale with an objective scattering reference. We determine the temperature factor ($B = -1000\,\text{Å}^2$) and derive noise-dependent structure factor weights required to correct the structure factor amplitudes without amplifying noise. Features of the potential map of the E2 catalytic core thus obtained at 8.7 Å resolution using 3667 icosahedral particle images (220,020 asymmetric units) are similar to those of a structural model obtained by X-ray crystallography. Comparison of the map and X-ray model allows an independent assessment of the resolution of the map and confirms the success of the restoration procedures.

Theoretical Background

Guinier analysis

Proteins contain a hierarchy of structural features. Spherically averaging structure factor amplitudes in resolution shells emphasizes common resolution-dependent features of all proteins and facilitates comparison with reference structure factors or theoretical scattering criteria. Analysis of the structure factors of a three-dimensional potential map determined by electron microscopy may be treated in the same framework as that used to study the spherically averaged structure factor data obtained in solution scattering experiments using X-rays or neutrons. In addition, spherical averages of structure factor correlations between independent maps are the basis of resolution assessment and signal-to-noise estimation in single-particle analysis.

Reciprocal space structure factor amplitudes of a protein span several orders of magnitude as a function of resolution. A Guinier plot shows the natural logarithm of the average structure factor as a function of resolution ($1/d^2$). Figure 1 presents a schematic Guinier plot of a protein consisting of two regions: (1) a steeply descending shape/solvent-dependent region at low resolution; and (2) a relatively flat secondary structure/random atom region at high resolution.

At the lowest resolution, the amplitudes are determined by the shape of the protein contrasted against solvent. In the Guinier approximation,[9] applicable to resolutions $d \sim 2\pi R_g$, where R_g is
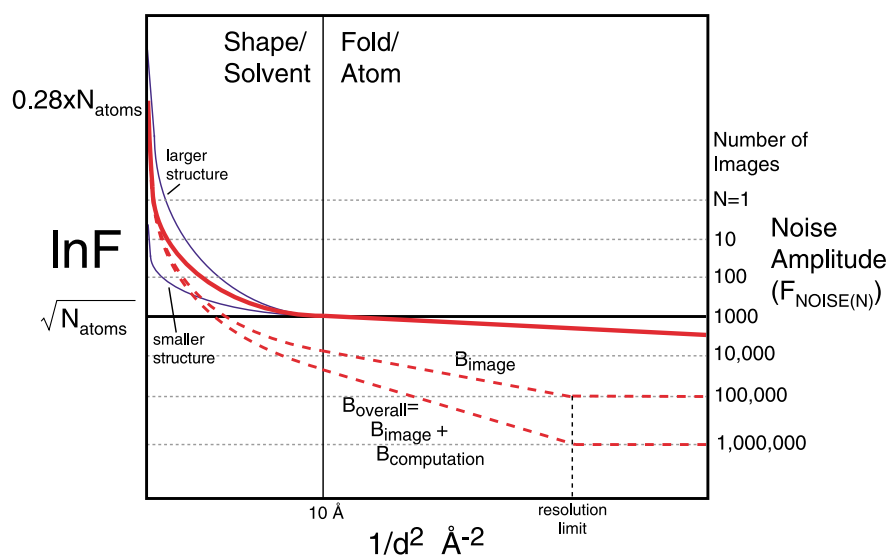
Figure 1. Schematic Guinier plot shows the natural logarithm of the spherically averaged structure factor amplitude (F) for a protein against $1/d^2$, where d is the resolution (Å). Zero angle scattering is equal to N_{atoms} carbon equivalents of the molecular mass multiplied by the solvent contrast (0.28) and places the scattering on an absolute scale. The protein scattering curve (red line) consists of a low-resolution region ($d > 10$ Å) determined by molecular shape and solvent contrast, and a high-resolution region ($d < 10$ Å) which approaches the scattering of randomly placed atoms described by Wilson statistics, which decreases only slightly with resolution and may be approximated by the horizontal line of amplitude $\sqrt{N_{\text{atoms}}}$. The high-resolution region may also have structure corresponding to fold-specific features, including α-helix and β-sheet. The average noise amplitude is $F_{\text{Noise}(1)}$ for a single image or $F_{\text{Noise}(1)}/\sqrt{N}$ after averaging N images. Low-resolution structure factor amplitudes are also shown for a large structure that might be studied by tomography and a small molecular mass particle which has a low-resolution scattering amplitude below the noise level for one image (blue lines). The experimental contrast loss for structure factors at high resolution due to imperfect images is indicated by a dotted red line labeled by its slope, the temperature factor B_{image}. Additional contrast lost due to imperfect computations gives a line with slope B_{overall}, which is the sum of temperature factors B_{image} and $B_{\text{computation}}$. The resolution limit is indicated where the structure factor curve equals the noise level, which in this example occurs at 10^6 particles for B_{overall}, but at 10^5 particles if $B_{\text{computation}} = 0$.

the radius of gyration, the scattering amplitude is described by:

$$F = (\rho - \rho_0)V_{\text{protein}}e^{-(2\pi^2 R_g^2/3d^2)}$$

where $(\rho - \rho_0)$ is the difference in scattering density between protein (ρ) and solvent (ρ_0). When written in terms of protein atomic scattering factors f_i:

$$F = ((\rho - \rho_0)/\rho)(\sum_i n_i f_i)\, e^{-(2\pi^2 R_g^2/3d^2)}$$

The scattering maximum occurs at zero angle ($d = \infty$) where all atoms scatter in phase and is equal to $\sum_i n_i f_i$ multiplied by the solvent contrast term $(\rho - \rho_0)/\rho$. The mean structure factor amplitude is large but decays rapidly with resolution and continues to reflect shape and solvent to about 10 Å.

Beyond 10 Å, the mean scattering amplitude depends to some extent on protein-specific features including fold and secondary structure, but on average is determined by the essentially random position of atoms in the interior of the protein. According to Wilson statistics,[10] the average scattering amplitude from randomly positioned atoms is given by $F = \sqrt{\sum_i n_i f_i^2}$. This average amplitude decreases slowly with resolution roughly in line

with individual atomic form factors, but is essentially constant when compared to decay in the shape/solvent region at lower resolution. Predominantly α-helical structures tend to have stronger diffraction around 10 Å resolution, whereas those with larger amounts of β-structure diffract more strongly around 4.5 Å, producing small deviations from Wilson scattering.

Experimental structure factor amplitudes may be placed on an absolute scale by setting the zero angle scattering equal to $((\rho - \rho_0)/\rho)N_{\text{atoms}}$ and average scattering amplitude in the Wilson regime equal to $\sqrt{N_{\text{atoms}}}$, where N_{atoms} is the number of equivalent atoms of identical scattering factor such that $N_{\text{atoms}}/\sqrt{N_{\text{atoms}}} = (\sum_i n_i f_i/\sqrt{\sum_i n_i f_i^2})$. For a typical protein, N_{atoms} may be determined by assuming the protein molecular mass is made up of N_{atoms} equivalent carbon atoms ($12 \times N_{\text{atoms}}$ Daltons). In this simplified model, the scattering amplitude at both low and high resolution may be expressed in terms of a single parameter derived from the molecular mass. The molecular mass of a protein is usually known in advance of structural study.

The solvent contrast factor $(\rho - \rho_0)/\rho$ is equal to about 0.28 for X-rays (assuming protein density ρ is 0.42 e$^-$/Å^3 in proteins and solvent ρ_0 is 0.30 e$^-$/Å^3 for ice of mass density 0.92 g/cm^3). When calculated

using neutral atom electron-scattering factors, $(\rho - \rho_0)/\rho$ is approximately 0.42.

Averaging particle images

The average noise level of a low-dose image limits the ability to record structure factors to a resolution given by the intersection of the protein amplitude curve with the average noise amplitude for one particle image. The amplitude of the average noise spectrum for one particle image can be placed on the absolute scale of the protein structure factors and is represented in Figure 1 as a line with amplitude $F_{\text{Noise}(1)}$. The ability to average images of identical particles increases the signal-to-noise ratio and makes high-resolution information accessible. When the amplitude of the noise after averaging N particle images is plotted on an absolute scale, this corresponds to a noise level $F_{\text{Noise}(N)} = (F_{\text{Noise}(1)}/\sqrt{N})$, where $F_{\text{Noise}(1)}$ is the noise level for one image. $F_{\text{Noise}(N)}$ is drawn for various numbers of images in Figure 1. The resolution achieved for a given experiment and a given number of images is therefore the point at which the protein structure factor amplitude equals the amplitude of the average noise level.

Coherent averaging of structure factors requires determination of particle orientations and positions on the film. Structure factors (reflecting both shape and higher-resolution features) above the noise level provide the signal used to determine orientations of individual particles. Since the structure factor is proportional to molecular mass, a particle of higher molecular mass will intersect the noise level at higher resolution than a smaller particle. A lower molecular mass threshold exists, perhaps around 50 kDa,[1] where the low-resolution signal does not reach above the noise level for a single low-dose image. In this case it will be impossible to determine the orientation parameters for the particle in order to average images of many identical particles.

The structure factor amplitudes at resolutions essential for alignment must not be attenuated by the microscope CTF. Defocus is used to increase contrast by enhancing low-resolution structure factor frequencies that are essential for alignment. Effects of high defocus include the introduction of zeroes in the structure factor transform and spatial displacement of structure factor spacings in the image.[11] The image must be corrected for these effects of the CTF, requiring coherent illumination and an accurate knowledge of the defocus and astigmatism.

Tomography

For specimens in which every particle structure is different, averaging many particles is not possible, and multiple projections must be obtained by tomography. The orientation of each projection relative to the others in the tomographic series is known. Therefore, the particle orientation parameters need not be determined in each micrograph, and a lower dose can be used to record each projection, but the number of images in the series is still limited by radiation damage. According to the dose fractionation theorem, the signal-to-noise ratio of a projection of the final reconstruction is not greater than if the total dose were used to record just the single projection.[12] The ultimate resolution of tomography is therefore limited to the intersection of the average structure factor amplitude with the noise level in a single image recorded with the total dose (See Figure 1, intersection of the structure factor amplitude with the noise level $F_{\text{Noise}(1)}$ for one image). A higher molecular mass object will intersect the noise level at higher resolution than a smaller particle. Tomographic reconstruction to ~ 20 Å for high molecular mass specimens is an important goal.[13] The limiting resolution of tomography may be estimated by extrapolation from the resolution and noise level obtained when averaging single-particle images to that obtained from one image. If low-resolution features tolerate a greater electron dose than high-resolution features, then use of a greater total dose than optimum for high-resolution, single-particle analysis may result in a further small improvement in the resolution predicted for cryotomography.

Loss of contrast

Experimental density maps determined by single-particle electron microscopy show a loss of contrast at high resolution. As elsewhere,[14] the contrast loss can be measured as the ratio of structure factor amplitudes of the experimental map and reference amplitudes. The reference amplitudes can be derived from a high-resolution X-ray structure or theoretical scattering criteria such as those described above.

The loss of contrast at high resolution is a property of the images, and therefore recording the best possible experimental images is essential. Factors which may degrade image contrast include specimen movement and charging, radiation damage, inelastic electron-scattering events, partial microscope coherence, and particle flexibility and heterogeneity.[14] The combined effect of these factors may be modeled by a Gaussian fall-off of structure factors at high resolution given by $e^{-(B_{\text{image}}/4d^2)}$ with temperature factor B_{image} as drawn in Figure 1.

The contrast may be decreased further by the inability of the computational procedures to extract and average the signal from the micrograph. The densitometer modulation transfer function (MTF) may contribute to contrast loss in the digitized image. The poor signal-to-noise ratio of the images makes computational determination of orientation parameters and microscope parameters difficult. Inaccurate or completely incorrect assignment of these parameters will blur features in the image in proportion to resolution or add noise in more

complex ways. This incoherent averaging causes a decline in contrast, which may be described by $e^{-(B_{computation}/4d^2)}$ as shown in Figure 1. The relative contribution of this computational loss of contrast may be difficult to distinguish from the experimental loss of contrast in the images themselves. The structure will have an overall temperature factor, $B_{overall}$, the sum of B_{image} and $B_{computation}$, which reflects all the factors which reduce contrast. Because the resolution limit of the structure is determined by the intersection of the average structure factor with the average noise level, a larger temperature factor requires averaging more particles to achieve a given resolution.

Contrast restoration

It is necessary to restore the high-resolution structure factor amplitudes of a map so that low and high-resolution terms have correct relative scaling (also called sharpening). The down-weighting of the high-resolution data due to contrast loss will make the map look relatively smooth and featureless. The experimental (positive) temperature factor describing the contrast loss can be measured with respect to a scattering reference on a Guinier plot. The amplitudes can then be corrected by applying a negative temperature factor ($B_{restore}$) in the form $e^{-(B_{restore}/4d^2)}$.[15] However, this type of simple sharpening will amplify the noise as well as the signal (signal-to-noise ratio unchanged). At high resolution where the signal has become weak, this will simply make the map noisier, so the amount of sharpening must be appropriately weighted according to the signal/noise present in the map at a given resolution.

The signal-to-noise ratio of the map may be derived from a common criterion for resolution assessment, the Fourier shell correlation (FSC).[16,17] In the Appendix we argue for a resolution criterion based on the estimated correlation between a map calculated from a full dataset and a perfect reference map containing no errors. This correlation, C_{ref}, may be calculated for a resolution shell as $C_{ref} = \sqrt{(2FSC/(1 + FSC))}$, where FSC is the correlation between two independent maps, each calculated from half the data. Also shown in the Appendix, C_{ref} is equal to the cosine of the average phase error and is equivalent to the crystallographic figure-of-merit,[18] a common measure of map interpretability in X-ray crystallography.

Because an experimental structure factor is the sum of both signal and noise components, we show in the Appendix that $C_{ref} = \sqrt{S^2/(S^2 + (N^2/2))}$ where S is the average signal amplitude and $N/\sqrt{2}$ is the average noise amplitude in the full dataset. At low resolution, where the structure factors are free of noise, $C_{ref} \sim 1$. At the resolution limit of the map, where $S \sim N$, C_{ref} becomes less than 1. Noise-weighted structure factors that are the product of C_{ref} and F will down-weight resolution shells containing noise.

Thus, as with the figure-of-merit weighting used in X-ray crystallography,[18] a map calculated using amplitudes multiplied by $C_{ref}\,e^{-(B_{restore}/4d^2)} = \sqrt{2FSC/(1 + FSC)}\,e^{-(B_{restore}/4d^2)}$ will be the best map.

Results

Microscopy and image analysis of E2CD

We chose the E2 catalytic core of the *B. stearothermophilus* pyruvate dehydrogenase complex as a test specimen for high-resolution, single-particle cryomicroscopy. Pyruvate dehydrogenase is a complex of up to 10 MDa containing three enzymes (E1, E2, E3) that catalyze the conversion of pyruvate to acetyl CoA and CO_2. The E2 protein is a dihydrolipoyl acetyltranferase and, depending on the organism, forms a cubic or icosahedral core of the complex through the oligomerization of its C-terminal catalytic domain (28 kDa). E2 also contains one or more N-terminal lipoyl domains and an E1/E3 binding domain connected by flexible polypeptide linkers.[19] X-ray studies[20] and electron microscopy studies[21] of a truncated form of the *B. stearothermophilus* E2 protein containing only the 28 kDa catalytic core domain (E2CD) show an icosahedral complex with 60 subunits and mass of 1.5 MDa.

High-resolution images of E2CD in ice were collected under low-dose conditions ($15-20\,e^-/Å^2$) at 300 kV on a microscope with a field emission gun. A range of defocus values ($2.3-7.7\,\mu m$) were included to fill in reciprocal space zeroes resulting from the CTF. All the defocus values were large to enhance low-resolution contrast helpful in finding particles. A similar strategy of using large defocus values will be essential in microscopy of lower molecular mass particles. We included the carbon support surrounding the ice holes in the image to reduce specimen charging[22] and to provide a source of strong scattering for an initial estimate of the defocus for the film. Particle coordinates on a digitized micrograph were selected manually and individual particle images were cut out in boxes. Typical particle images are shown in Figure 2(a) and (b).

We used a previously described 14.5 Å resolution map,[21] calculated by angular reconstitution from untilted images with subsequent refinement, as a starting point for model-based determination of orientation and microscope parameters of the single-particle images. The program FREALIGN[23] was used to refine parameters for individual images, correct for the effects of the microscope CTF, and to calculate three-dimensional electron potential maps. The orientation of a particle is described by three Euler angles (ψ, θ, ϕ) which give the relative orientation of the three-dimensional model corresponding to the image projection and the translation (x, y) describing the
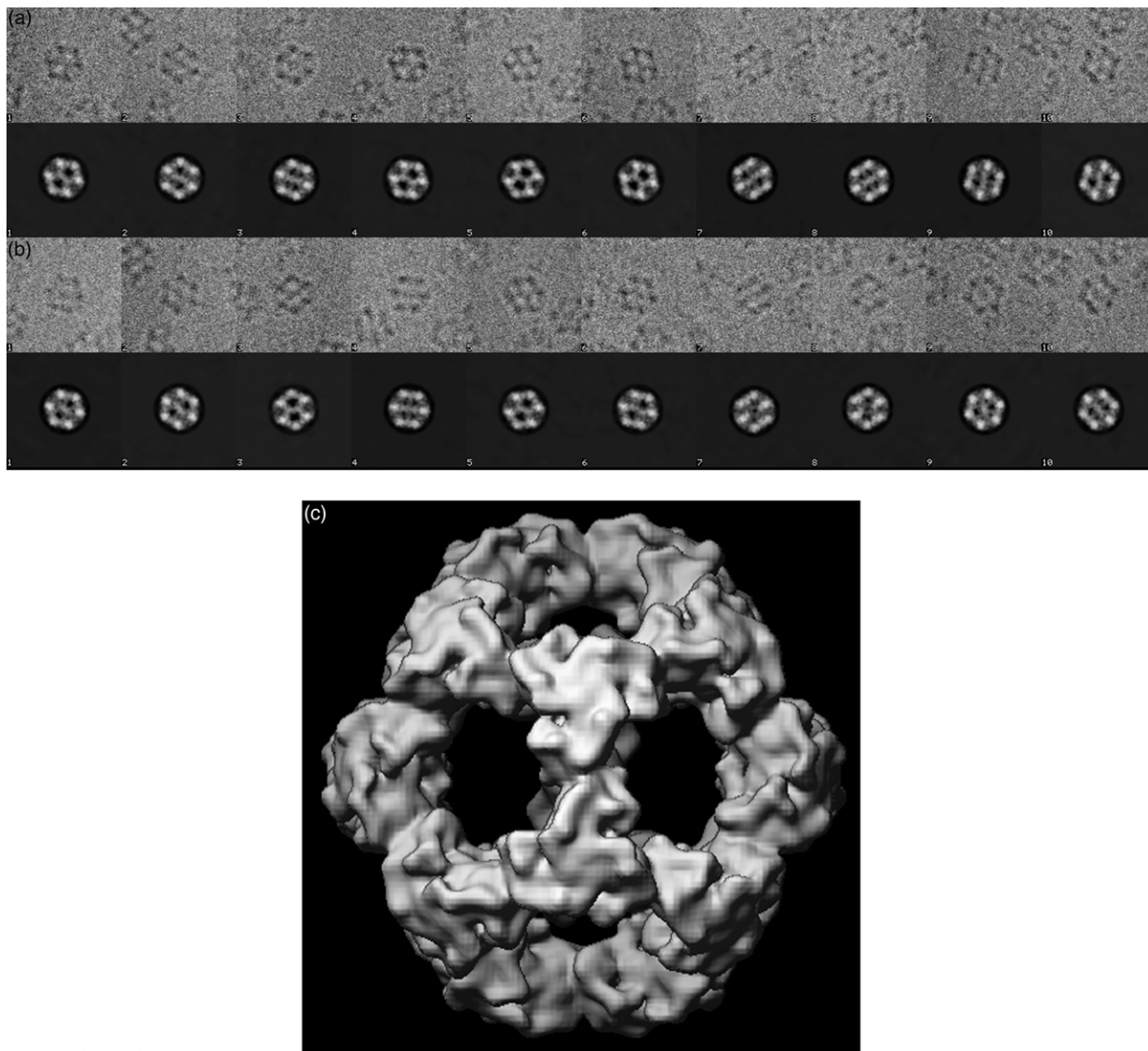
Figure 2. Images of *B. stearothermophilus* E2CD in ice at 59,000× magnification and a defocus of 5.9 μm. (a) Raw particle images selected from a film recorded with an untilted specimen holder and (b) the same particles from a second film recorded with the specimen holder tilted by 10°. (c) Model used to determine particle orientations and to calculate projections matching the particle orientations shown in the bottom rows of (a) and (b).

location of the center of the particle projection. Microscope parameters for individual particles include the magnification and three parameters describing defocus ($\Delta F1$, $\Delta F2$, and the angle of astigmatism). The quality of the reconstruction ultimately depends on the correct assignment of the particle orientations and microscope parameters. During iterative model refinement, the images are first corrected for the effects of the CTF, and then particle orientations or microscope parameters are refined by improving the agreement between calculated model projections and CTF-corrected images. A better model should therefore lead to more accurate determination of particle orientations and microscope parameters. When more accurate microscope parameters are used in CTF correction, the subsequent refinement of particle orientations will be more accurate.

CTF-correction is performed on raw images by first multiplying image transforms by the CTF which includes both phase and amplitude contrast terms (see the equation given in the legend to Table 1), and is a function of three image-specific parameters $\Delta F1$, $\Delta F2$, and the angle of astigmatism. An effect of defocus (ΔF) is to displace image spacings of resolution d by a distance $\lambda\Delta F/d$, where λ is the electron wavelength.[24] In order to include all the information, the raw image box size was chosen to be $D + 2R$, where D is the particle diameter and R is the displacement expected for the most defocused image at the maximum resolution spacing expected in the reconstruction. In reciprocal space, the effect of multiplying by an accurately determined CTF is to invert image phases which are of the wrong sign due to the microscope transfer function, enhance frequencies near CTF maxima, and attenuate frequencies near zeroes of the CTF. The effect in

Table 1. Effect of orientation refinement parameter on absolute hand determination

Refinement parameter Data resolution (Å)		Film 1 score	Film 2 score (data 100–35 Å) at phase residual minimum			
Min	Max	ϕ_{untilt}	Tilt angle	$\phi_{freehand}$	$\Delta\phi_{freehand}$	
100	35	35.7	7.5	48.53	6.50	
80	25	44.2	11.5	43.86	16.32	
80	20	51.1	10.6	43.40	16.72	
80	15	60.5	10.8	43.25	16.65	
80	35	34.8	7.0	45.70	5.90	
45	20	62.0	-	46.44	14.48	
300	20	49.8	10.8	43.41	16.32	
80	[a]15	46.8	10.0	43.05	17.04	
Map quality						
Map 006		49.5	10.0	42.97	15.46	
Map 031		49.5	10.0	42.99	15.63	
Map (Figure 1(c))		46.3	10.0	40.76	17.06	

Refinement parameter (data resolution range) was varied in determining orientations of 50 particle images from untilted film 1 and scored with average phase residual ϕ_{untilt}. Orientations on film 1 were then scored for agreement against 50 particle images from tilted film 2. The scores on film 2 include the tilt angle, average phase residual at the minimum corresponding to the correct hand ($\phi_{freehand}$, the "free hand phase residual"), and the difference between the average phase residual at the correct hand and the incorrect hand ($\Delta\phi_{freehand}$, the "free hand difference"). Different maps were compared after optimizing all refinement parameters below. Values for refinement parameters influencing orientation determination after optimization: reconstruction radius: 146 Å. Resolution range: 100–15 Å. Number of cycles of randomization and refinement: 200. PBC = 100, BOFF = 35, DANG = 200. Fraction amplitude contrast WGH: 0.07 (see following CTF equation). $CTF = -\sqrt{1 - WGH^2}\sin\chi - WGH\cos\chi$, where $\chi = 2\pi/\lambda\left(\frac{\Delta F\theta^2}{2} - \frac{C_s\theta^4}{4}\right)$, C_s is the spherical aberration of the objective lens (2.0 mm), θ is the diffraction angle λ/d, and the defocus ΔF in direction Φ_{obs} is $\Delta F = \Delta F_1\cos^2\Phi + \Delta F_2\sin^2\Phi$, where ΔF_1 and ΔF_2 are the amounts of defocus in two orthogonal directions, $\Phi = \Phi_{obs} - \Phi_{angast}$, and Φ_{angast} is the angle with defocus ΔF_1.
[a] Refinement temperature factor $\exp(-B_r/4d^2)$ B_r, 3000 Å^2.

real space is to convolute image densities with the Fourier transform of the CTF, which moves displaced image spacings back to their true location in the specimen projection. A real space circular mask with a cosine edge is applied to the CTF-corrected image and the additional non-centered particles beyond the reconstruction radius seen in Figure 2 do not influence subsequent processing. The transform of the three-dimensional reconstruction is computed by interpolating and summing the two-dimensional transform of each image at lattice points determined by the particle orientation (ψ,θ,ϕ), and normalizing each lattice point by dividing by the sum of (CTF)^2 for all images contributing to the lattice point.[23] After averaging images at a variety of defocus values, the resulting structure factor profile should be directly comparable to that expected in a theoretical Guinier plot for the specimen.

The agreement between a projection calculated from a model and an image is given by the amplitude-weighted phase residual between the Fourier transform of the CTF-corrected image and the Fourier transform of the calculated model projection, $PR = \sum_i |\Delta\phi F_i| / \sum_i |F_i|$, where $\Delta\phi$ is the phase difference and F_i is the amplitude of the image structure factor. The value of the phase residual depends on the accuracy of the orientation and microscope parameters, the resolution range over which it is calculated, and also on the noise level and particular view of the particle in the image. However, a low value for the phase residual can reflect a fit between the model projection and noise, and is not in itself a guarantee of accuracy in orientation refinement.

For a given model, orientations and microscope parameters were refined by Powell minimization with the phase residual as a target.[23] Refinement parameters that influence the determination of particle orientations are listed in Table 1. These include the resolution range of the data, a refinement temperature factor B_r which determines the relative weight of high and low-resolution data according to $e^{-(B_r/4d^2)}$, the reconstruction radius, and the relative weight of amplitude and phase contrast terms in CTF correction. Additional parameters control further details of the refinement strategy. In particular, we chose a refinement strategy in which the particle orientations were randomized and then minimized a specified number of times to avoid local minima and to speed convergence. In this study, the same microscope parameters were used for all the particles recorded on the same film.

A map based on 1681 icosahedral particles from 14 micrographs recorded independently of those used to make the starting model contained signal to 11 Å and is shown in Figure 2(c). Our initial choice of parameters controlling the refinement came from reasonable assumptions about their effects and the desire to avoid systematic bias in the refinement. The maximum data resolution for refinement was between the first and second zeroes of the CTF. Reconstructions were always calculated to a resolution higher than the resolution used in refinement. Signal in the map in these unbiased resolution shells not used for refinement was used to judge map improvement.

Absolute hand determination

The three-dimensional model of the E2 core complex described above was derived entirely from images of untilted specimens, and was therefore of unknown hand. Although the hand of the map could be compared to the hand of the X-ray model (see Comparison with X-ray model), we sought to develop an automatic procedure to determine the absolute hand using a pair of micrographs recorded with the specimen at two tilt angles relative to the electron beam. The application of a tilt transformation to the orientations determined for untilted particles gives a predicted orientation

for the tilted particles. If the model is of correct hand, its projection should agree with the image of the tilted particle after rotating by the tilt angle used in the experiment. If the model is of opposite hand, its projection will agree with the images after rotation by the negative of the tilt angle. The agreement can be scored by the phase residual.

Micrographs were recorded first from an untilted specimen and then from the same specimen tilted by 10.0°. Fifty particles present in both micrographs were selected, several of which are shown in Figure 2. The orientations of untilted particles were determined as described in the last section. Tilt transformations $\{rot_x, rot_y\}$ (see Methods) in 1° increments up to ±15° covering all possible directions and tilt angles for the goniometer were applied to the orientation of each untilted particle to produce a set of predicted orientations for each particle corresponding to each one of the 961 tilt transformations. The phase residual for each of these tilt-transformed orientations (after re-optimizing the particle translation x,y) was determined on the tilted particle image. The phase residual for each tilt transformation was then averaged for 50 particles and shown in the contour plot in Figure 3(a). Though a tilt pair for one particle can show a phase residual minimum sufficient to determine the absolute hand, some particle images may give an incorrect conclusion, and it is therefore better to average a statistically significant number of particles.

Since the specimen was tilted by +10° to obtain the second micrograph, a minimum should occur at a tilt angle of either +10° (if the model has the correct hand), or −10° (for the incorrect hand). Only an approximate knowledge of the tilt axis direction on a micrograph at a given magnification is necessary for determining absolute hand in this procedure (see Methods for a detailed protocol for determining which tilt transformation corresponds to the microscope tilt axis direction and polarity). The position of the minimum phase residual, 49.5°, at co-ordinates of (+7, +2) corresponds to the known direction and polarity of the microscope tilt axis, and demonstrates that the handedness of our three-dimensional model is correct. The average phase residual for the opposite hand at (−7, −2) is higher by 7.8° than the correct hand (called the "free hand difference"). However, the minimum in the plot corresponds to a tilt angle of 7°, which differs from the known tilt angle of 10° used in the experiment. Because the goniometer rotation is accurate to 0.1°, the fact that the minimum is not precisely at 10° indicates that the Euler angle determinations may not be correct for all the particles.

## Use of absolute hand to optimize the determination of particle orientations

We next tested whether the systematic under-estimate of the true tilt angle in absolute hand determination was caused by errors in the deter-
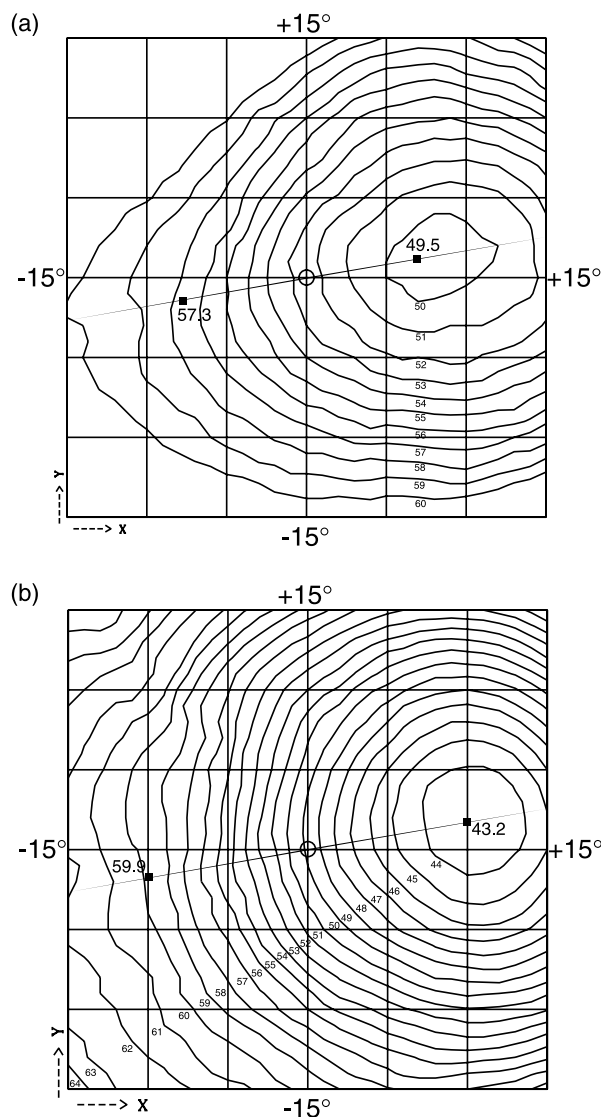
Figure 3. Determination of the absolute hand of E2CD. Average phase residuals for 50 particle images recorded at a tilt of 10° were determined using the 3D model and tilt-transformed orientation parameters of the corresponding untilted particle images. The contours show phase residuals for tilt transformations up to 15° along the x and y axes. A vector from the origin to any point in the map corresponds to the direction of the tilt axis and its length is the tilt angle $= \sqrt{x^2 + y^2}$. The direction of the known tilt axis of the microscope is shown as a black diagonal line. (a) Black squares indicate that the phase residual for the model shown in Figure 2(c) has a minimum (49.5°) near the rotation angle of the experiment (7°) and a lower value than for the negative rotation (57.3°), indicating that the hand of the model is correct. (b) Same as (a) after parameter optimization according to Table 1. The minimum (43.2°) is lower and occurs at a rotation angle of 10°. The discrimination of correct from incorrect hand or "free hand difference" is 16.7° (compared to 7.8° in (a)).

mination of particle orientations. Inaccurate or incorrect particle orientations could result from non-optimal choices of the refinement parameters that influence orientation determination. Some
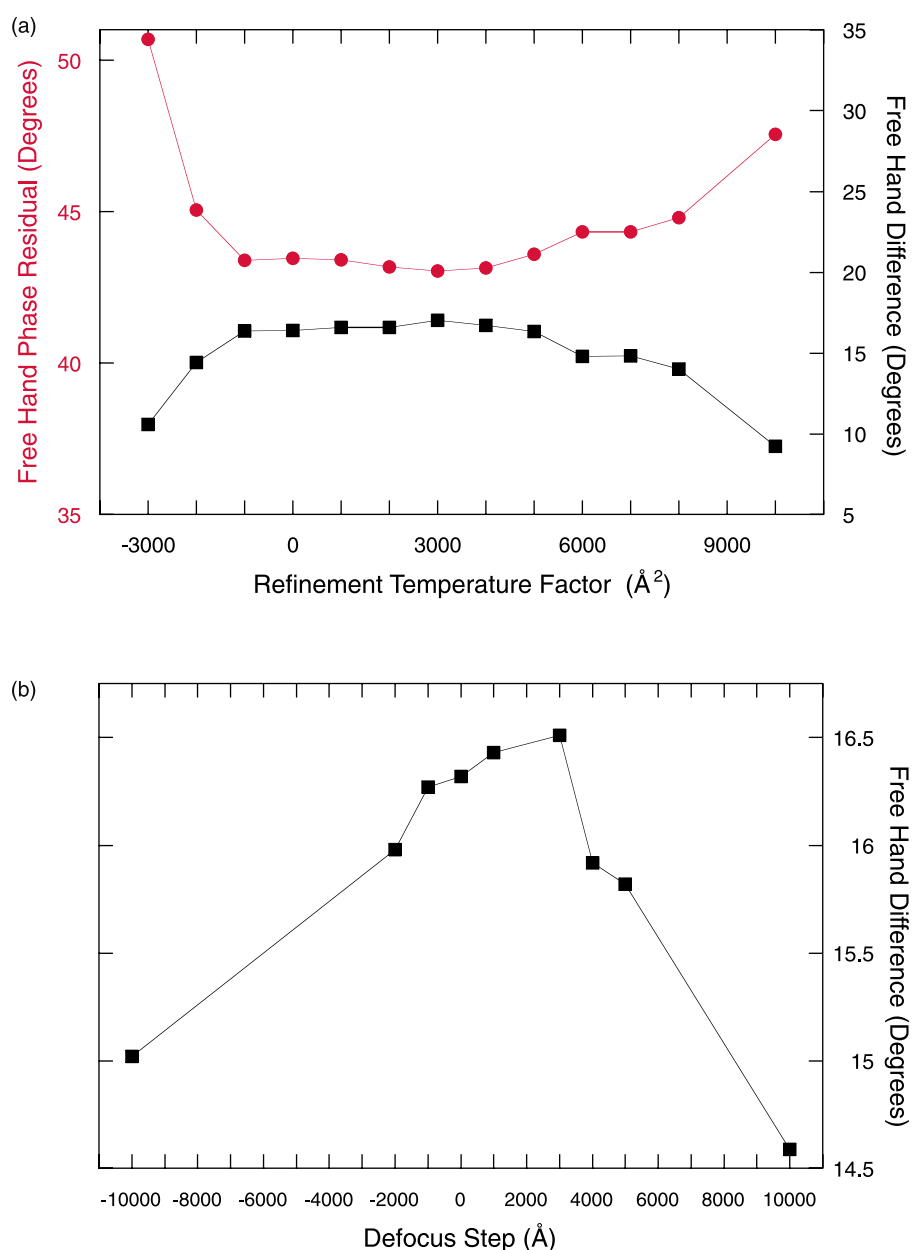
Figure 4. Optimization of parameters influencing orientation determination. (a) Refinement temperature factor (B_r). Free hand phase residual minimum and free hand difference maximum occur at a B_r of 3000 Å². (b) Effect of variation of defocus ΔF on free hand difference showing a maximum at 0.3 μm change from starting value of 5.9 μm.

choices for refinement parameters were better able to discriminate the correct hand of the map from the incorrect hand. We systematically varied the refinement parameters when determining orientations for the untilted particles only (Table 1 and Figure 4). The accuracy of the orientations of the untilted particles for a given choice of refinement parameter was then assayed on the tilted particle images. For the tilted particles, phase residuals for all tilt transformations were calculated with a constant choice of parameters using image data to low resolution ($r_{min} = 100$ Å and $r_{max} = 35$ Å) so that the resulting phase residuals could be directly compared with each other.

The difference between the phase residual at the correct and incorrect hand (the "free hand difference")

ence") as well as the depth of the minimum at the correct hand (the "free hand phase residual") were used as targets for optimizing all the parameters influencing orientation determination. In addition, the true tilt angle and tilt axis are known during the experiment and are the same for all particles on the pair of micrographs, making them objective targets for optimizing refinement parameters which influence orientation determination and which affect the calculated tilt axis and tilt angle given by the location of the minimum phase residual. All parameters listed in the legend to Table 1 were varied in determination of the orientations of the untilted particles.

As shown in Table 1, our results demonstrate that data resolution limits (r_{min} and r_{max}) are critical.

When $r_{\min} = 100$ Å and $r_{\max} = 35$ Å, the free hand phase residual is 48.5°, the free hand difference is 6.5°, and the minimum occurs at an angle of 7.5°. When $r_{\min} = 80$ Å and $r_{\max} = 20$ Å, the free hand phase residual drops to 43.4°, and the free hand difference increases to 16.7°. In this case the calculated tilt angle from the data is 10.6°, much closer to the actual tilt angle of 10°. The better agreement with the target values and its correlation with better free phase residuals suggests better orientation determination when including higher resolution data.

In Figure 4, we show further optimization of two parameters. The refinement B-factor, B_r, which increases or decreases the weighting of higher-resolution data in the image, was varied between

-3000 Å^2 and $+12,000$ Å^2. A minimum occurs at 3000 Å^2 as shown in Figure 4(a). This indicates that optimal orientations are found when the data at 15 Å ($r_{\max}$) are attenuated by a factor of 20, reducing the effect of noise at high resolution in the images. In Figure 4(b), the optimization of a microscope parameter, the defocus, is also shown to influence the free hand difference and the accuracy of orientation determination.

Figure 3(b) shows the phase residual map after applying the optimization procedure for all refinement parameters in Table 1. A much lower and more symmetrical phase residual minimum (43.2°) occurs at coordinates $(+10, +2)$ and corresponds to a 10° rotation around the known direction and polarity of the microscope tilt axis. The free hand
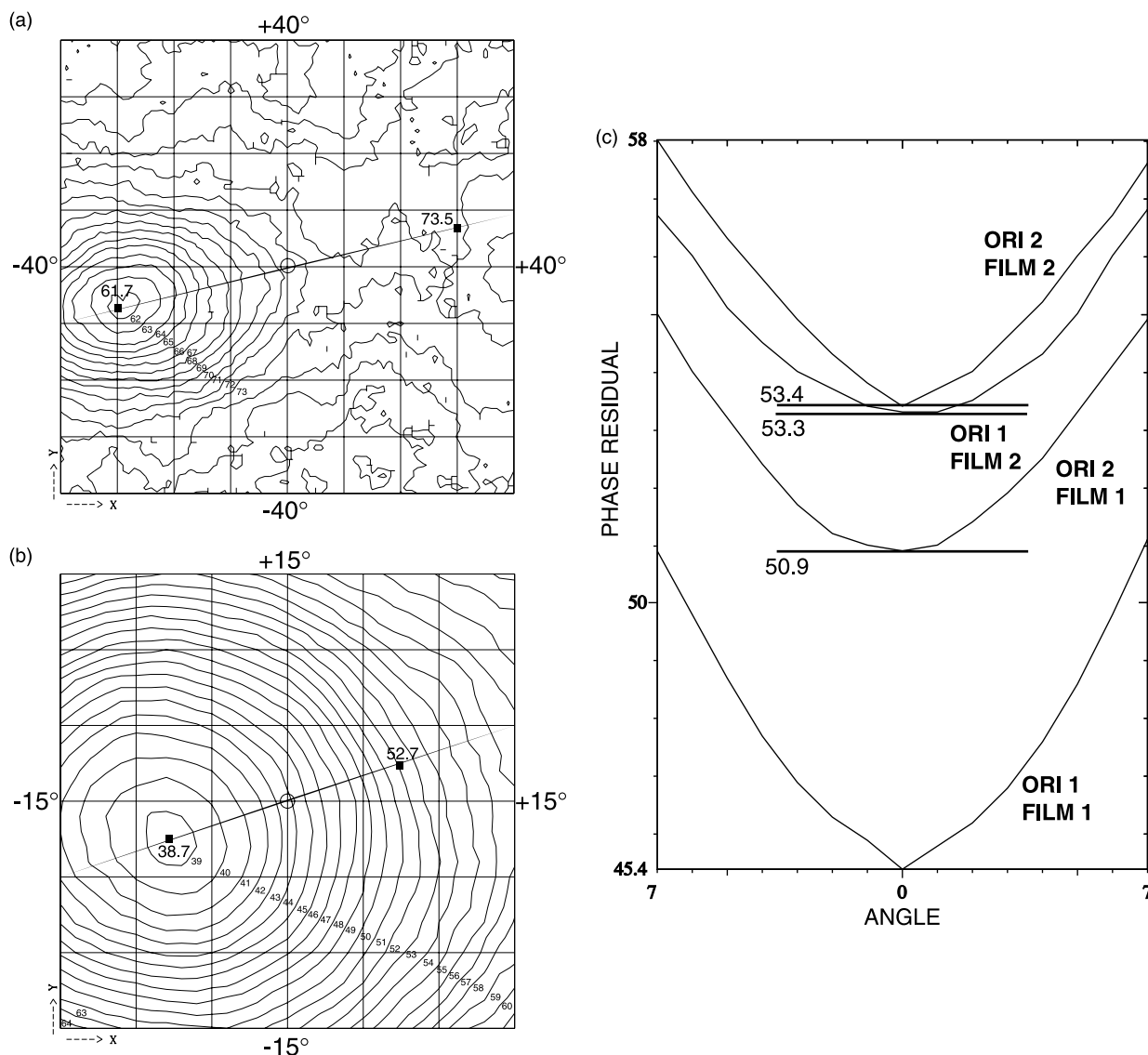

Figure 5. (a) Absolute hand determination as in Figure 3, but with a relative tilt angle of 30° (recorded at ±15°). The +15° tilted film was recorded first, so the phase residual minimum occurs at −30°. (b) Hand determination for 10° tilt using the second exposed tilted film to determine the hand on the first untilted film. (c) Phase residual for model against a pair of images of the same particle field recorded without tilting. The tilt-transformed orientation parameters for each film (labelled ORI 1, ORI 2) were scored against either film 1 or film 2. Tilt angles up to 7° about a single axis are shown.

difference (16.7°) is much higher than with the initial parameters used in Figure 3(a). Using these optimized refinement parameters, the scores for absolute hand determination also depend on the quality of the three-dimensional map, as shown in Table 1 for several maps calculated over the course of the structure determination. The improvement in a map at high resolution can also be demonstrated by evaluating the minimum phase residual at the correct hand as a function of resolution.

Hand determination using large tilt angles is likely to experience all the problems associated with images of tilted specimens, such as defocus gradients and greater charging. We have shown that our procedure works successfully for tilt angles of 5–10°, where these problems are expected to be minimal. For large tilt angles, however, the change in particle view is more dramatic giving a larger free hand difference and, in principle, a greater sensitivity for the optimization of parameters. A large tilt angle also makes the hand determination procedure a sensitive measure of particle flattening. We have recorded images at a variety of tilt angles and in Figure 5(a) we show the hand determination using the same optimized refinement parameters for particle images from two micrographs recorded with a relative tilt angle of 30(±15°). The tilt angle calculated through hand determination is 29.4° and was 30.8° for a second independent experiment. We therefore conclude there is no evidence for flattening of particles during sample preparation for cryomicroscopy, nor from the effects of irradiation and likely mass loss, both of which would result in an apparent underestimate of the tilt angle.

The same hand determination procedure can be performed by first determining orientations for the tilted particles and then scoring the orientations against the untilted particles. The resulting contour plot (using the same data as Figure 3(b)) is shown in Figure 5(b). Now the minimum should occur for a −10° rotation (since changing the order of the films is equivalent to changing the sense of rotation). However, using optimized parameters, the calculated rotation angle is −7.5°, rather than −10°, indicating less accuracy in orientation determination. In other cases where both micrographs were recorded from tilted specimens, first film orientations as scored by phase residuals on the second film were as good as those where the specimen was initially untilted. This suggests that poor orientations on the second film are not the result of tilting *per se*, but are the result of radiation damage. To further demonstrate the effect of radiation damage on orientation determination, we recorded two consecutive micrographs of the same particle field without tilting, in which case orientations on the two films should be identical, excluding particle movement.

After determining orientations for particles on the first film, we calculated the effect of applying a single-axis rotation to the orientations and scoring the average phase residual for particle images on the same film in the data range $r_{min} = 100$ Å and $r_{max} = 35$ Å (Figure 5(c)). For orientations determined on the second film and scored against the second film, the average phase residual is higher at the minimum (53.4°) than for first film orientations scored against the first film (45.4°), and the variation of phase residual with tilt angle is shallower, suggesting that orientations are on average less well-defined. When orientations determined on the second film are scored against the first film, the phase residual is lower on the first film (50.9°) than the second (53.4°), but is not as low as with orientations determined on the first
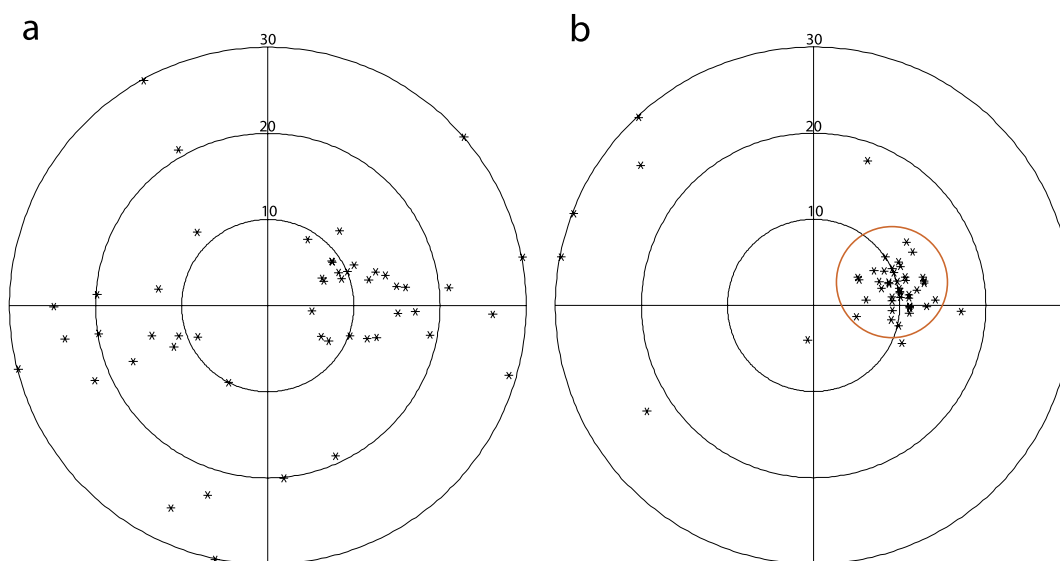

Figure 6. Determination of tilt axis for each particle pair. Particle orientations were determined separately for particles on the untilted and 10° tilted films. The best tilt axis relating orientations on the untilted and tilted film are plotted for each particle before (a) and after (b) optimization according to Table 1. Tilt axes within the red circle have an RMS deviation of 3.2°.

film (45.4°). The increased phase residual for orientation determination on the second film reflects the fact that the images themselves have poorer agreement with the model even at low resolution, but also that orientation determination on the second film is less accurate, probably because of the damage to higher-resolution features.

As a final demonstration of the improvement in particle orientation resulting from parameter optimization, we used an entirely different approach requiring the separate determination of the orientations of the untilted and tilted particles. For each particle, the best tilt axis was found that relates the untilted and tilted particle orientations with the constraint that it lies in the plane normal to the electron beam (see Methods). We plot the tilt axis direction and tilt angle for each particle pair before (Figure 6a) and after (Figure 6b) optimization using the same data and refinement parameters as used in Figure 3(a) and (b). As shown by the clustering at the known target

values, the tilt axis and angle are also more accurately determined in Figure 6b on an individual particle basis. Orientations are therefore more accurately determined after optimization. The RMS deviation for the well-clustered tilt axes (within the small circle in Figure 6b) is 3.2°. The error for the tilt axis reflects errors in orientation on both films, but the error in orientation on a single film is the most important quantity to know for most data collection strategies. For example, if orientations have two times worse RMS error on the second film than on the first because of radiation damage, then the RMS orientation error in orientations on the first film is approximately 1.4°. Using Figure 6 it is possible to identify individual image pairs for which the tilt angle is incorrect. Removing images that are clearly outliers due to noise features, damage, or particle heterogeneity may also improve hand discrimination by the free hand difference.

In summary, the ability to determine absolute
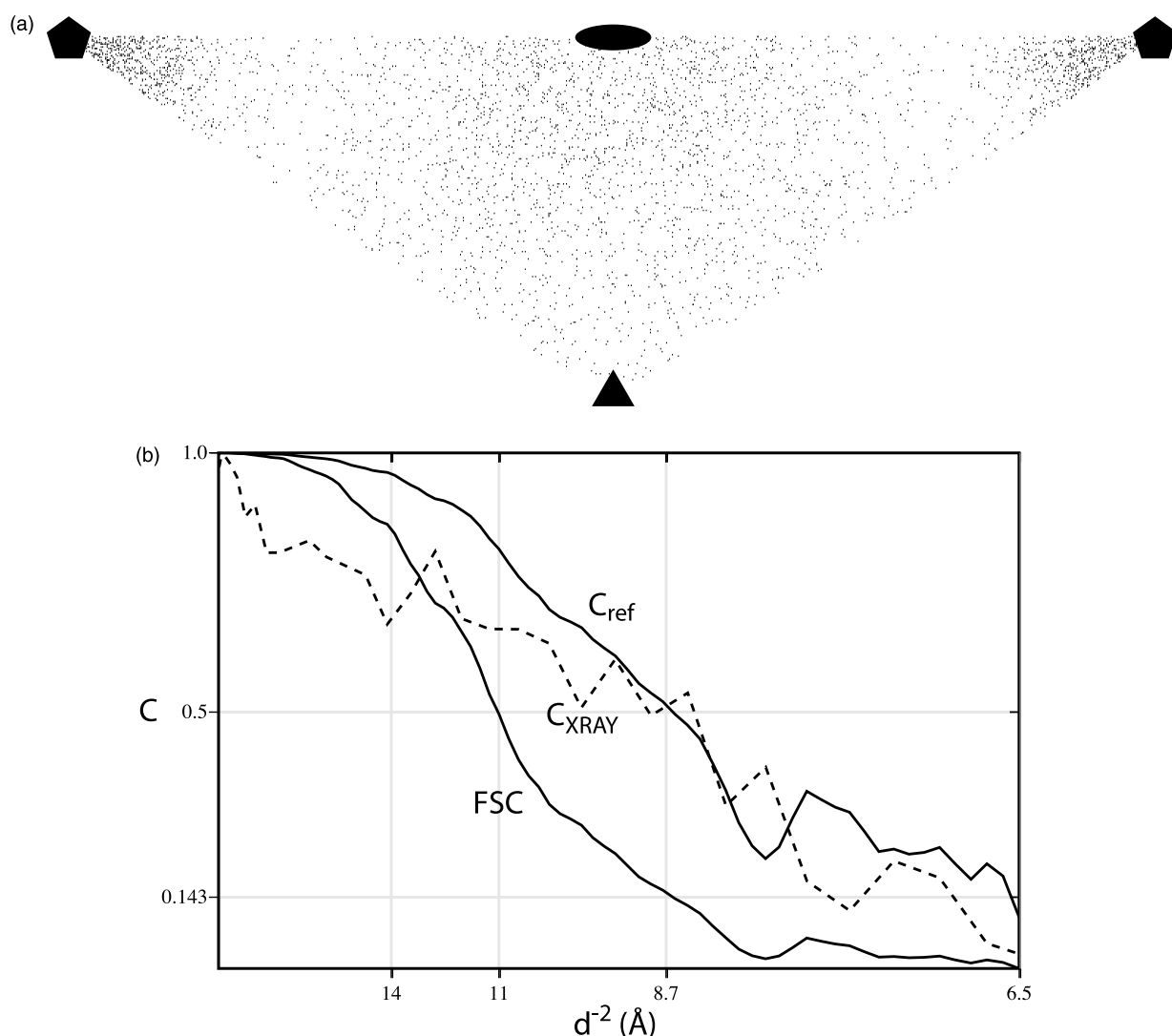
Figure 7. Data for the final E2CD map. (a) Distribution of orientation angles for particles, with 5, 3, and 2-fold symmetry axes labeled. (b) Fourier shell correlation (FSC), C_{ref}, and C_{XRAY} for the final dataset.

hand depends on accurate orientation determination. By using the free hand difference, tilt angle, and tilt axis as targets for rapidly optimizing the parameters that influence orientation determination, the accuracy of the orientations improved. Orientation determination is influenced by noise, and each image in a tilt pair will have different noise features. With the refinement parameters optimized by hand determination, the minimum phase residual discriminates between the real image features and the noise. Better orientations produce a better map at higher resolution by reducing the computational temperature factor ($B_{computation}$).

Contrast loss and restoration

We have applied the optimized procedures for the refinement of particle parameters to a dataset of 3667 untilted images of icosahedral E2CD and calculated a map. The orientations for all the particles are shown in Figure 7(a). We plot the Fourier shell correlation (FSC) for the map in Figure 7(b). The FSC is the correlation between two independent maps, where each map is calculated from half the images. In the Appendix, we argue that the resolution of the map should be assigned at the point where the FSC crosses a threshold of 0.143. This corresponds to the resolution at which the estimated correlation between a density map calculated from all the data and a perfect reference map ($C_{ref} = \sqrt{(2FSC/(1 + FSC))}$), also plotted in Figure 7(b)) is 0.5. C_{ref} is equivalent to the crystallographic figure-of-merit, a common measure of map

interpretabiliy in X-ray crystallography. The resolution of the map is thus 8.7 Å.

We now assess high-resolution contrast loss in the experimental map by comparing spherically averaged structure factor amplitudes to a scattering reference as shown in the Guinier plot in Figure 8. The reference structure factors are computed from an X-ray model of the complex (see the next section for details on the model) assuming a background solvent density of $1.0 \, g/cm^3$. Both experimental and calculated structure factors are placed on an absolute scale by setting the zero angle scattering equal to the product of the solvent-contrast term (0.28) and N_{atoms}, the number (136,100) of carbon atom equivalents corresponding to a molecular mass of the complex (1.5 MDa). The experimental structure factor amplitudes have a similar average value to the reference at low resolution where scattering is dominated by the shape and solvent contrast of the complex. Small differences likely result from the inability to model solvent adequately in the reference. At high resolution the amplitudes decay considerably from the relatively flat profile of the reference. Also shown is a horizontal line of amplitude $\sqrt{N_{atoms}}$ representing the average scattering amplitude of randomly positioned atoms given by Wilson statistics, a reference criterion for structure factor amplitudes at high resolution.

In Figure 8, we also plot noise-weighted structure factors, $C_{ref}F$, where C_{ref} is calculated from the FSC after smoothing (noise-weighted amplitudes can be calculated up to the resolution at which the weighting function C_{ref} becomes random and the amount of signal in the data becomes negligible).
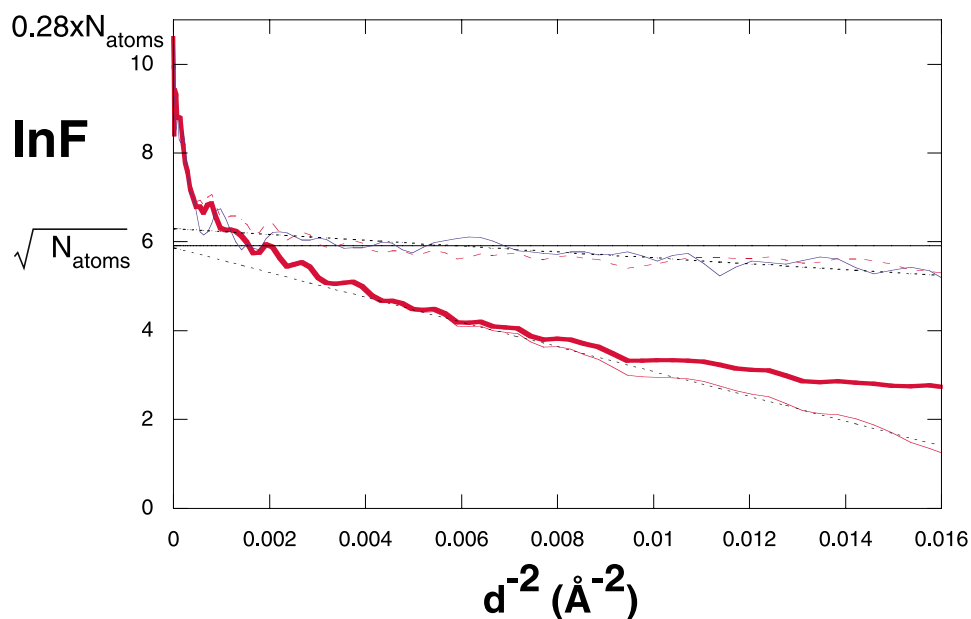
Figure 8. Guinier plot showing the natural logarithm of the spherical average of *F versus* $1/d^2$ for the experimental map (thick red line), the experimental map amplitudes weighted by C_{ref} (thin red line), weighted amplitudes after sharpening (broken red line), Wilson statistics (horizontal black line), and the X-ray model (blue line). Linear fit of data for $1/d^2$ between 0.005 and 0.015 yields $B = 1200 \, Å^2$ for the experimental map and slope $200 \, Å^2$ for the model structure factors (dotted black lines). The difference, $B = -1000 \, Å^2$, is used to sharpen the experimental map.
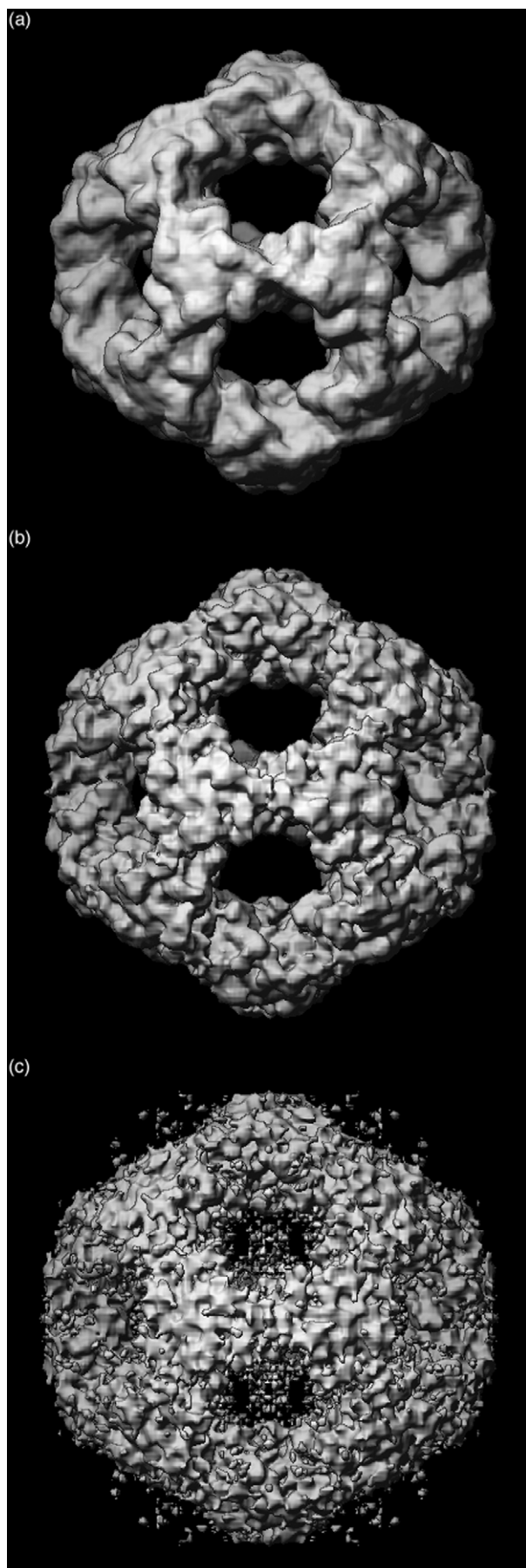
$C_{\mathrm{ref}}F$ better represents the average signal in the map, particularly at and beyond the resolution limit of the map where signal becomes proportional to noise (see Theoretical Background). The weighted curve shows a more linear, monotonic fall-off over a wider resolution range, consistent with the high-resolution amplitude decay being modelled by a single temperature factor. It is therefore possible to measure more accurately the temperature factor at the resolution limit of the map. The straight line fitted to the linear part of the noise-weighted amplitude curve at high resolution indicates a temperature factor of 1200 Å^2 compared to the flat line representing Wilson statistics. It may be noted that the linear fit to the decay intersects zero angle at $\sqrt{N_{\mathrm{atoms}}}$, the amplitude given by Wilson statistics. This is also consistent with modelling the high-resolution structure factors by Wilson statistics and a single temperature factor.

Over the same resolution range, the X-ray model structure factors decay by an amount equivalent to a temperature factor of approximately 200 Å^2 compared to Wilson statistics, due to features of the molecular fold and the decline of scattering factors. The amplitude decay compared to the X-ray model is therefore best described by a temperature factor of 1000 Å^2. For resolutions greater than 10 Å, the extent to which the true structure factors for any given protein deviate from Wilson statistics is likely to be small, and a general correction for the observed decay in all proteins may suffice. The estimate of the temperature factor can therefore be made for proteins for which no known reference structure or scattering curve exists.

To observe molecular details at the resolution limit of the map, it is necessary to correct the structure factor amplitudes for the loss of contrast. We multiply the noise-weighted structure factor amplitudes $C_{\mathrm{ref}}F$ by $e^{-(B_{\mathrm{restore}}/4d^2)}$, where B_{restore} is a temperature factor of -1000 Å^2. Figure 8 also shows the spherically averaged structure factor amplitudes of the resulting sharpened map. Figure 9 shows a comparison of the unsharpened map (Figure 9(a)), the sharpened map with noise-weighted structure factor amplitudes (Figure 9(b)), and a map obtained by applying the same temperature factor to unweighted structure factors (Figure 9(c)), all calculated to 8.0 Å.

The sharpened map shows detailed molecular features not present in the unsharpened map as further analyzed in the next section. In the map calculated without weighted structure factors, noise is amplified to an extent that produces extraneous detail. A map calculated to the nominal resolution of 8.7 Å without noise weighting looks similar to the 8.0 Å map with noise weighting,

Figure 9. Effects of sharpening ($B_{\mathrm{restore}} = -1000$ Å^2) on maps calculated to 8.0 Å: (a) unsharpened; (b) sharpened, noise-weighted structure factors; (c) sharpened, unweighted.

since the application of the precise resolution threshold removes terms where there is little signal contributing to the map. With noise-weighted structure factors the map is insensitive to the chosen resolution cut-off of the map and potentially contains molecular features beyond the nominal resolution limit of the map. In addition, noise-weighted structure factors will be less sensitive to over-sharpening due to errors in temperature factor estimate, and little difference was observed in maps calculated with a B_{restore} of -1000 Å^2 or -1200 Å^2. Given an electron potential map and a measure of the signal as a function of resolution (C_{ref}), the appropriate calculation to restore contrast is determined without bias by the data itself.

Comparison with X-ray model

The potential map of E2CD determined by electron cryomicroscopy was compared to high-resolution crystallographic models of the catalytic core. A 2.3 Å X-ray structure has been reported for the E2 catalytic domain of *Azotobacter vinlandii* (PDB 1eea), which is a cubic form of the enzyme containing eight copies of a basic trimer structural unit.[25,26] *A. vinlandii* and *B. stearothermophilus* share 40% sequence identity in the catalytic core. A structure for the dodecahedral *B. stearothermophilus* catalytic core has been reported based on 4.2 Å crystallographic data and molecular replacement using the *A. vinlandii* trimer (pdb 1b5s), demonstrating that the trimer can form quasi-equivalent interactions in cubic and icosahedral symmetry.[20] However, in that study, the limited resolution or quality of the data prevented the refinement of the *B. stearothermophilus* model, and the resulting structure is a homology model and does not contain side-chains. Because the available icosahedral *B. stearothermophilus* X-ray model lacked side-chains, we superimposed the *A. vinlandii* monomer on each of the 60 monomers of *B. stearothermophilus* and calculated structure factors, spherical averages of structure factors, and map density for comparison with the results of cryomicroscopy. At the resolutions under investigation, the mass distribution is important, but the identity of the side-chains is unimportant.

The experimental map (Figure 10(a)) and X-ray model were compared by aligning icosahedral symmetry elements which uniquely define the model location without further fitting, except for a 3% adjustment of the magnification of the map. Overlap with the model and density is shown in Figure 10(b) and (c). The model and map possess the same absolute hand. Helices are clearly resolved at this resolution as shown in the stereo diagram of the density covering a single monomer in Figure 10(d). β-Sheets are apparent but individual strands are not differentiated. The map also differs from the model in loop regions, and some portions of the model may require refitting for optimum placement in the map density.

Density for residues N-terminal to Gly204 is absent or appears at very low contour (Figure 10(d)). In the *A. vinlandii* structure these residues extend away from the monomer and interact with adjacent monomers in the trimer. These residues are the least conserved between *A. vinlandii* and *B. stearothermophilus* and could be in a different conformation or disordered. This observation is consistent with these residues being part of an extended mobile linker connected to the E1/E2 binding domain.[21]

Comparison of the appearance of the cryomicroscopy potential map and electron density maps computed from the model suggests that the features of the map are in agreement with corresponding X-ray maps computed between 8 Å and 9 Å resolution and confirms the resolution assessment. The correlation between the map and X-ray model (C_{XRAY}) is shown in Figure 7(b) and has similar values whether X-ray or electron form factors are used. In principle, C_{XRAY} should be similar to the correlation (C_{ref}) between the full image dataset and a perfect reference. C_{XRAY} is 0.46 at a resolution of 8.7 Å where C_{ref} is 0.5. When structure factors calculated from the X-ray model includes scattering from a flat bulk solvent of 0.3 e$^-$/Å^3, C_{XRAY} is 0.51.

Discussion

The structure of the icosahedral E2 catalytic core of the pyruvate dehydrogenase complex from *B. stearothermophilus* has been determined to 8.7 Å resolution by electron cryomicroscopy and image analysis of 3667 untilted icosahedral particles (220,020 asymmetric units). Images were recorded at high defocus on a field emission gun microscope at 300 kV and corrected for the effects of the CTF. Model-based refinement was used to determine the orientation parameters of the particles and microscope parameters for each image.

An advantage of our choice of E2CD as a test object for a critical analysis of single-particle techniques is that an X-ray structure is known, allowing direct confirmation of the success of the methods for reconstruction, contrast restoration, and resolution assessment. The structure looks similar to an electron density map computed from an X-ray model for E2CD from the 40% sequence identical *A. vinlandii*. Some differences likely reflect real features of *B. stearothermophilus* E2CD. Structural studies of multi-enzyme complexes such as pyruvate dehydrogenase are essential to understand how the geometric arrangement of the protein subunits determines their complex reaction kinetics.[19,21]

In the course of the work, we have sought to develop unbiased procedures for addressing two fundamental issues in the image analysis of single particles. The first concerns how best to determine the particle orientation in an image. Our initial attempts at hand determination of E2CD using the

736 Single-particle Cryomicroscopy
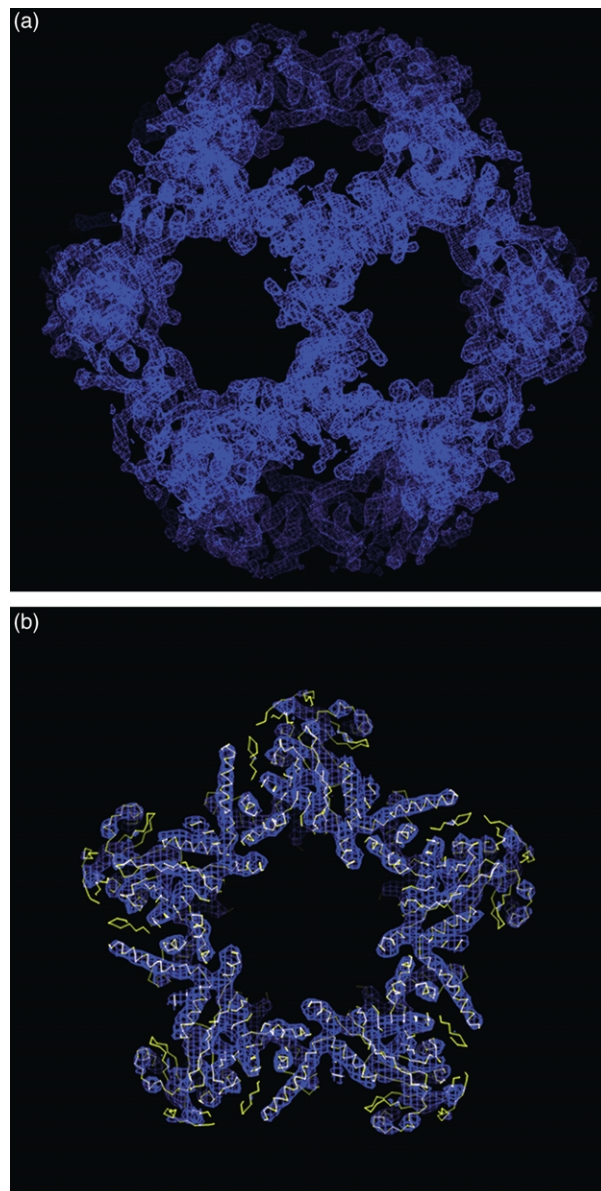
**Figure 10 (a) and (b)** (*legend opposite*)

best images showed that more accurate orientations were required. We showed that hand determination could be used to optimize refinement parameters leading to better orientations and therefore a better map. Once a map is obtained, the second issue is how the decay of structure factor amplitudes at high resolution can be restored.

Absolute hand determination is important in interpreting structures determined by high-resolution electron microscopy of single particles because the chirality of a biological molecule is the basis of its function. We have developed a semi-automatic procedure for hand determination requiring a model and two image stacks corresponding to particles from a single pair of low-dose images recorded at two angles of a tilt axis. We used the procedure on a molecule of known

hand, demonstrating that we have chosen the right conventions throughout the image processing steps that are capable of inverting the hand.

The hand determination procedure maps out the average phase residual for all possible tilt axes based on the agreement of tilted particle images with orientations predicted from untilted particles. A minimum is expected at the known tilt angle and axis of the experiment. The confidence of the hand determination is measured by the difference between the score at the tilt angle corresponding to the correct hand and the score at the negative tilt angle corresponding to the opposite hand (here called the free hand difference). A confident result for hand determination depends on accurately determining particle orientations. A given refinement strategy based on the mini-mization of the phase residual between model
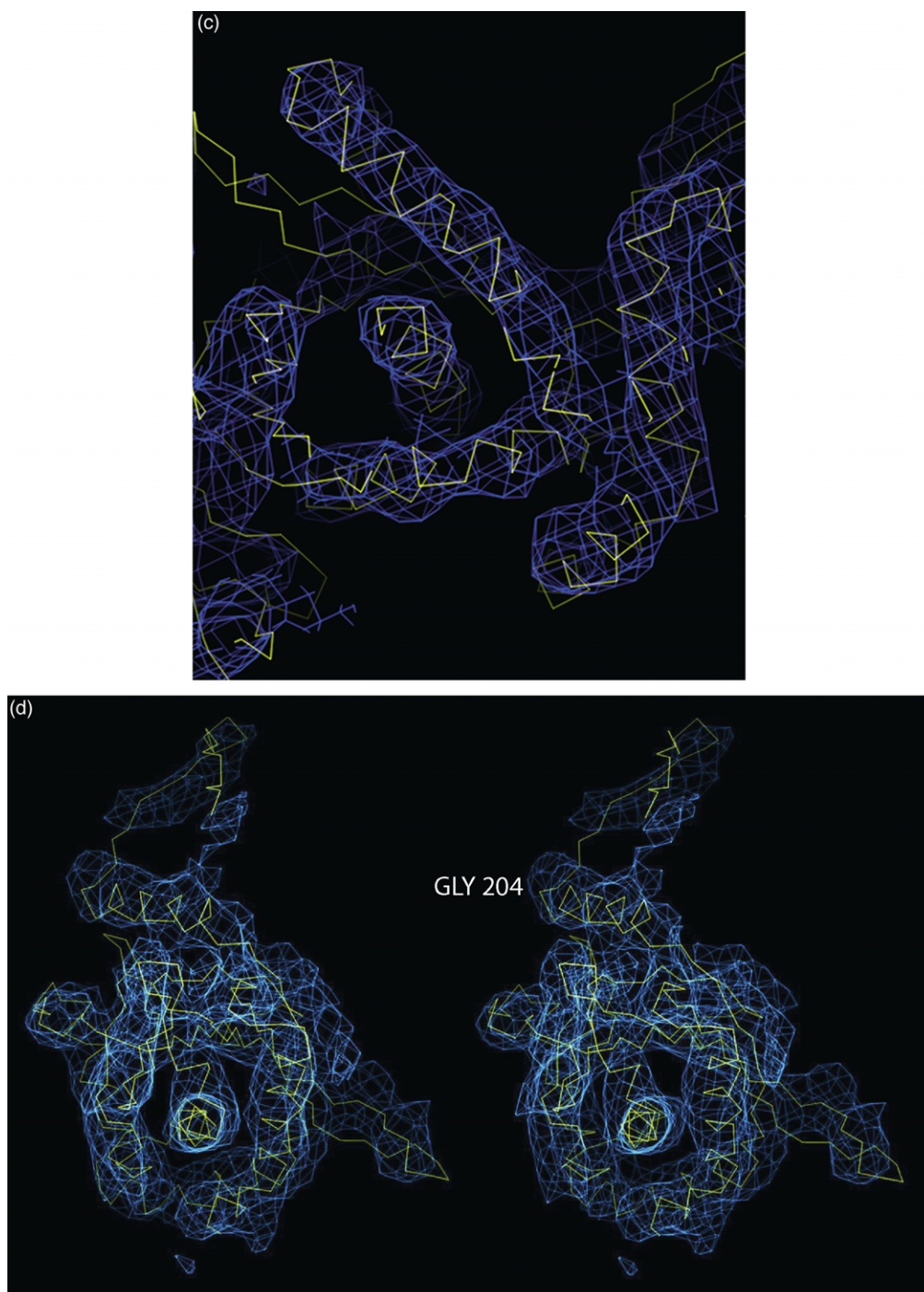
Figure 10. Experimental map density for E2CD. (a) Final map density viewed down a 2-fold axis. (b) Final map density with superimposed coordinate model viewed down the 5-fold axis. (c) Close-up view of map density on the coordinate model. (d) Stereo view of monomer density on the model with the location of Gly204 labelled.

projection and image may be influenced by noise features in the image rather than signal. For a known tilt angle and tilt axis, the particle orientation should change in a predictable way, but the noise should be uncorrelated. The success of orientation determination on the first film can be assayed on the second film, independent of the noise or spurious features on the first film. The known tilt angle, tilt axis, and free hand difference are unbiased targets for optimizing the parameters that influence the accuracy of orientation determination. Since the accuracy of microscope parameters is shown to influence orientations, microscope parameters may also be refined by this method. All refinement parameters can thus be rapidly and systematically tested on a single pair of images, but the results may be applied to all images in the dataset. In the absence of such a procedure, the arduous task of repeated structure determinations to high resolution with variation of

all parameters would be required. Because hand determination is ultimately a test of the consistency of the model with the data, it can be used to test the quality or validity of a model, and possibly identify particle heterogeneity in a dataset by detecting image pairs that together are inconsistent with a model. A second tilted image could routinely be included in an automatic data collection strategy to identify particle heterogeneity or damage.

We have shown that individual particle orientations are better determined after the parameter optimization using absolute hand. Particle orientations need to be well-determined, because averaging images inaccurately or incoherently leads to blurring of high-resolution features or to contrast decay. It is still an open question whether the orientations are well enough determined for structure determination to atomic resolution.[27] If the particle orientations are determined with perfect accuracy, then the remaining contrast loss is an intrinsic property of the images. Because the measured tilt angle is the same as the known tilt angle of the experiment for large relative tilt angles up to 30°, there is no evidence for flattening during sample preparation and exposure in the electron beam, suggesting that cryomicroscopy can provide high-resolution structures without artifacts. Nevertheless, radiation damage does destroy high-resolution features and reduces the accuracy of orientation determination. In the future, recording particle images on electronic detectors with high-resolution pixels may lead to more accurate orientations through fractionation of the accumulated dose on separate frames and determination of resolution-dependent weights for each frame.

We have shown that contrast restoration is essential to reveal the highest-resolution molecular features of the electron potential map. We estimated the structure factor amplitude decay by comparison of spherically averaged structure factors with reference structure factors using a Guinier plot. The structure factors were put on an absolute scale by setting the zero angle scattering equal to the molecular mass times a solvent contrast factor. Structure factor averages at resolutions beyond the shape/solvent scattering region are roughly flat and approach Wilson statistics. Therefore, an approximate theoretical scattering curve may be used as a reference without the need to perform a small-angle X-ray scattering experiment.[28,29] The large temperature factor measured for maps obtained from single particles is unlikely to be sensitive to small deviations in the true structure factors from the average reference scattering curve for typical proteins. We have modeled the loss of contrast by a single temperature factor. However, a more complex decay function may ultimately be required.

The application of a negative temperature factor will amplify both signal and noise. We applied a correction to amplitudes of the form $C_{ref}F \, e^{-B_{restore}/4d^2}$, where C_{ref} is the estimated corre-lation of the map with a perfect reference, and $B_{restore}$ is the negative temperature factor. In the Appendix we argue that C_{ref} is the best objective weight to apply to the electron potential map and is equivalent to the crystallographic figure-of-merit. C_{ref} can be expressed in terms of the FSC between data half-sets and is a measure of the data quality as a function of resolution. Noise-weighted structure factor amplitudes $C_{ref}F$ directly represent the signal in the data, give a less noisy estimate of the temperature factor, and down-weight noise during contrast restoration. The contrast restoration is therefore determined in an objective way by the observed amplitude decay and the quality of the data as a function of resolution.

Extrapolating the number of particles required to high resolution

To reach the ultimate goal of a high-resolution map that may be interpreted in terms of an atomic model, many more images are required. The number may be extrapolated from the experimental structure factor amplitude decay curve. Near the resolution limit of the map, this decay may be modelled by a single temperature factor $B_{overall}$. As described earlier (see Theoretical Background), the intersection of the average structure factor amplitude with the noise level determines the resolution of the features that can be observed, and the number of particle images determines the noise level. The amplitude decay curve reaches the noise level at 8.7 Å (FSC = 0.15). The structure factor amplitude ($F = 100.5$) at this resolution is equal to the amplitude of the noise after averaging 3667 experimental particle images. The noise amplitude for one image or for N images may then be determined by observing that $F_{Noise(N)} = (F_{Noise(1)}/\sqrt{N})$. In this sense, any amplitude value on the structure factor decay curve at any resolution may be expressed in terms of the number of particles required to reach that resolution.

In Figure 11, the straight-line fit of the amplitude decay curve with $B = 1000 \, \text{Å}^2$ is plotted against resolution with the structure factor amplitude expressed in equivalent particle numbers. Because $B_{overall}$ was calculated by comparing reference structure factor amplitudes with the final experimental map amplitudes, which include all the factors that degrade contrast in the experiment and in the calculations, the estimate of the number of particles required at each resolution reflects intrinsic image and densitometry defects as well as errors in particle parameters and in reconstruction algorithms. Improvement of any of the experimental or computational factors that contribute to contrast loss will lead to a smaller temperature factor and will produce higher resolution with fewer images. Also shown in Figure 11 (dotted lines) are the estimated number of particles assuming temperature factors with two, four, and eight times slower fall-off with resolution. These curves have
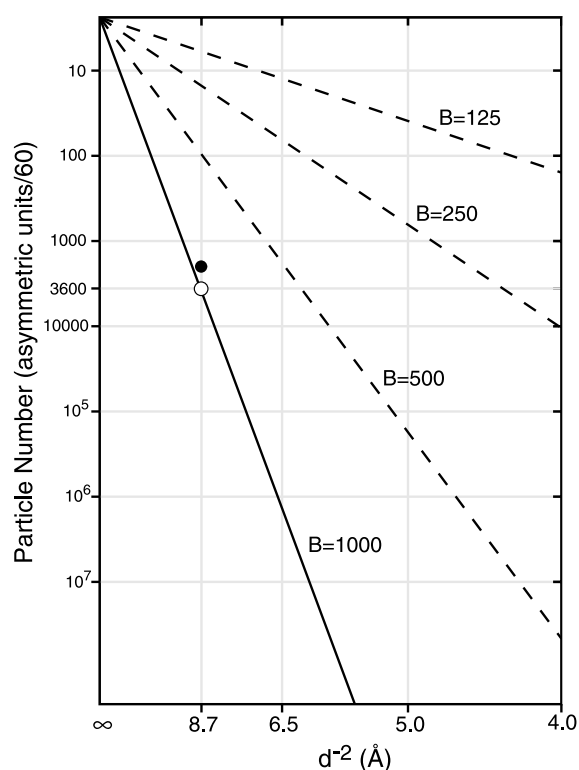
Figure 11. Estimate of the number of icosahedral images required as a function of resolution. The continuous line with $B = 1000$ Å^2 is the fit of the amplitude decay in Figure 8, but with the amplitude expressed in particle numbers. A single point (white circle) represents the resolution of the map obtained in this study with 3600 particle images. Calculated curves (dotted lines) for 500, 200, and 125 Å^2 assume the same zero angle intercept in agreement with Wilson statistics. Theoretical estimate of the number of particle images $N_{part} = (1/N_{asym})[(\langle S \rangle^2/\langle N \rangle^2)30\pi/N_e\sigma_e d]$ e$^{B/2d^2}$ required to 8.7 Å resolution assuming $\langle S \rangle/\langle N \rangle = 1/\sqrt{3}$ and $B = 1000$ Å^2, $\sigma_e = 0.004$ Å^2, $N_e = 5$ e$^-$/Å^2, and $N_{asym} = 60$ is 2200 particles (black circle).

an identical intercept at zero angle ($d = \infty$) where the temperature factor has no effect and which corresponds to the amplitude expected for Wilson statistics.

The extrapolated noise level ($F = 6028.8$) for one particle image intersects the average structure factor amplitude curve in Figure 8 at about 30 Å, well above the average amplitude given by Wilson statistics, in the part of the amplitude curve dependent on the overall shape of the molecule and contrast against solvent. In theory, this also represents the limiting resolution that would be obtained from studying a similar structure by tomography and fractionation of the total dose. Tomography is likely to provide information on overall shape, but averaging similar structures is essential to obtain higher resolution features.

The number of particle images used to reach 8.7 Å resolution in this study may be compared with recent theoretical estimates.[1,30] In one such estimate,[1] the number of images, N_{part}, required to

a resolution d is given by $N_{inproj}(\pi D/N_{asym}d)$ where N_{inproj} is the number of images needed for the average structure factor intensity in each projection to reach a threshold signal-to-noise ratio, and $\pi D/N_{asym}d$ is the number of unique projections for a particle of diameter D containing N_{asym} asymmetric units. Because the signal-to-noise ratio of the average structure factor in an image is the same as in the corresponding electron diffraction pattern,[14] N_{inproj} may be estimated by requiring a minimum signal-to-noise ratio for the average structure factor intensity of the electron diffraction pattern. N_{inproj} is given by $(\langle S \rangle^2/\langle N \rangle^2)/(((\langle I_{obs} \rangle/I_o)D^2N_e)$, where $\langle S \rangle^2/\langle N \rangle^2$ is the average number of electrons required in each structure factor (noting that a single electron recorded in a structure factor has a signal-to-noise ratio of 1), and the denominator is equal to the number of electrons in the average structure factor in a single low-dose image. The incident number of electrons is D^2N_e where $N_e = 5$ e$^-$/Å^2 is the allowed dose and D^2 is the area of the particle (or unit cell), and $\langle I_{obs} \rangle/I_o = \sigma_e/30D$ is the mean structure factor intensity as a fraction of the incident number of electrons,[1] where $\sigma_e = 0.004$ Å^2 is the elastic cross-section for carbon at 300 kV.[31] Thus the total number of particles $N_{part} = (1/N_{asym})((\langle S \rangle^2/\langle N \rangle^2)30\pi/N_e\sigma_e d)$. Previously, a 3σ criterion for the signal-to-noise ratio on amplitudes $(\langle S \rangle^2/\langle N \rangle^2 = 10$, where $\langle S \rangle$ and $\langle N \rangle$ are the signal and noise for the map computed from all the data) was chosen as a conservative criterion for estimating N_{inproj}, and the images were assumed to have perfect contrast. In the present study, we have shown that a resolution criterion related to map interpretability has $\langle S \rangle/\langle N \rangle = 1/\sqrt{3}$ at the resolution limit of the map. This reduces the number of images required to any given resolution by a factor of 30. In addition, the effect of contrast loss described by Gaussian decay leads to an increase in the required number of images by a factor $(e^{(B_{overall}/4d^2)})^2$. For $B = 1000$ Å^2 measured in this study, the theoretical estimate of the number of particles for 8.7 Å is 2200 particles, slightly more than half the number used in the experiment, 3667 (Figure 11).

The theoretical calculation assumes an electron dose of (5 e$^-$/Å^2) which is likely to be the limiting dose due to radiation damage for features near atomic resolution. The electron dose used in the experiment (18 e$^-$/Å^2) is three to four times this limiting dose. While the extra dose does not contribute to structure factor amplitudes near atomic resolution, it may have enhanced the signal up to the resolution limit of the final map and made determination of particle parameters easier. If the experimental electron dose is used in the calculation, the number of particles required by theory to 8.7 Å is decreased by a factor of 3–4, and the number of experimental images then exceeds the theoretical number by a factor of 6–8, even after accounting for the loss of contrast by a Gaussian fall-off. The best way to determine the more

complex function that models experimental contrast loss is to measure the build-up of image amplitude as a function of time, dose, and resolution by fractionation of the accumulated dose during image acquisition.

Though still a large assembly, E2CD is smaller than a number of icosahedral complexes solved to better than 10 Å by electron microscopy.[32,33] We have used highly defocussed images, such as will be required to extend higher-resolution studies to smaller particles. The large temperature factor may be a consequence of the large defocus (coherence envelope), but there may also be other imaging imperfections that depend inversely on particle size, such as beam-induced movement or image blurring. Particle heterogeneity could also contribute to the temperature factor. Given the excellent quality of the map, we have so far not attempted classification of the E2CD particles with the intent of identifying any conformational heterogeneity, such as has been reported for the mammalian enzyme[34] nor have we assessed its contribution to the overall temperature factor.

A 4 Å resolution map in which a protein model can be constructed cannot be achieved with realistic amounts of data of a quality comparable to that used here. It will therefore be necessary to obtain better quality micrographs with a decreased overall temperature factor. More accurate computation of particle orientations and microscope parameters will contribute by reducing the computational portion of the temperature factor ($B_{computation}$). It will be essential to reduce the intrinsic amplitude decay of images (B_{image}) by reducing movement and charging. Such improvements will lead to higher-resolution structures and will open a wide range of membrane proteins and macromolecular assemblies that are difficult to study in the crystalline state to structural and dynamical analysis by single-particle electron microscopy.

Methods

Electron cryomicroscopy

Purified *B. stearothermophilus* dihydrolipoyl acetyltransferase inner core, a 60-mer of the 28 kDa acetyltransferase domain comprising residues 173–427 of the E2 chain,[35] was a gift from Gonzalo J. Domingo and Richard Perham. Samples (3 mg/ml) in 50 mM sodium phosphate buffer, pH 7.0 were stored at −70 °C, and were diluted 1:10 (v/v) in PBS (phosphate-buffered saline) immediately prior to use. Holey carbon films were prepared as described[36] on 400-mesh Cu/Rh grids and glow-discharged for ten seconds in air: 2 µl of protein solution was applied to the carbon film in a high-humidity chamber,[37] blotted for 20 seconds with filter paper to remove excess sample, and plunged into liquid ethane at −180 °C. Grids were stored in liquid nitrogen and transferred to a Gatan cold stage. Images of particles over holes were recorded under low-dose conditions ($15–20\,e^-/Å^2$) on an FEI F30 microscope operating at 300 kV with 70 µm condenser and 50 µm objective aper-

tures, 59,000× magnification, and a defocus range between 2.3 µm and 7.7 µm.

Image analysis

Images were digitized on a Zeiss-SCAI flatbed densitometer using a 7 µm step and processed using programs from the MRC package.[38] Particles were selected manually using Ximdisp, boxed using LABEL and stored as one image stack per film. Image densities were floated to zero average. For images recorded at 60,000× magnification, adjacent pixels were averaged 4 × 4 with a resulting resolution of 4.98 Å/pixel in 128 × 128 pixel squares or averaged 2 × 2 with a resolution of 2.49 Å/pixel: 1681 particles from 14 films were included in the first dataset and 3667 particles from 26 films recorded at 300 kV were used in the final dataset.

Map refinement

Particle orientation parameters were determined first using a previously described 3D model[21] but were improved with successive rounds of refinement using FREALIGN.[23] Orientation and translation parameters for each particle image were determined each cycle by finding the minimum phase residual (see the text) with the model calculated using parameters from the last cycle. Two hundred cycles of particle orientation randomization followed by Powell minimization were used to determine the new orientation parameters. Parameters controlling the refinement are given in Table 1. To speed refinement, the five-orientation parameter search was conducted on particle images in a 128 × 128 pixel box at 4.98 Å/pixel, and the maximum resolution of data used in refinement was 15 Å. For maps calculated to resolutions higher than 15 Å, the x, y parameters only were re-refined against particle images in a 256 × 256 pixel box at 2.49 Å per pixel. Initial defocus parameters ($\Delta F1$, $\Delta F2$, and angle of astigmatism) for the CTFs used to correct the image structure factors were determined using CTFFIND2.[38] Both the CTF and magnification were refined using the same values for all particles on a film. Particle orientations were given by the Euler angles (ψ, θ, ϕ) according to a described convention.[11]

Procedure for recording and digitizing pairs of images of tilted specimens

Each tilt pair was recorded at two goniometer angles taking care to observe the sense of rotation of the specimen tilt axis. A positive value of the relative tilt angle corresponded to a clockwise rotation of the specimen holder viewed along the direction of specimen insertion from the nitrogen dewar toward the tip. Tilt pairs were recorded at 21,000×, 29,000×, 39,000× and 59,000× magnification.

The orientation and polarity of the F30 microscope tilt axis on micrographs were determined by either of two methods: (1) recording the movement of markers on a grid as the specimen stage was translated into the microscope; or (2) observing whether Thon rings from the micrograph indicated the relative position of the specimen as up (overfocus) or down (underfocus) on either side of the tilt axis. The tilt axis may therefore be described as a right-hand rotation about a vector oriented with respect to the film number recorded on the micrograph, a feature of fixed geometry common to all micrographs on a given microscope.

Because the orientation of the tilt axis varies with magnification, the relative orientation of the microscope tilt axis on the film at different magnifications was further checked by comparing images of the same catalase crystal (a gift from John Berriman). The axis was found to be rotated by 90° in the film plane at 59,000× compared to other magnifications.

Films were scanned with a consistent orientation on a Zeiss SCAI film densitometer as judged by the marking numbers on the microscope negative. Corresponding particles were selected on both micrographs of the tilt pair, boxed, and stored in register in separate stacks (program LABEL). Inspection of the full image containing film numbers in our display software (Ximdisp) allowed the known direction of the tilt axis to be assigned as an approximate vector direction in our software coordinate system. The tilt transformation corresponding to this known tilt direction and polarity is then described by $\{rot_x, rot_y\}$ (transformation defined below). We confirmed that all rotation transformations of three-dimensional volumes (program FREALIGN, program ANGPLOT) gave the expected effect when calculated projections were displayed using Ximdisp.

Image analysis of tilt pairs

Particle orientations were then determined separately for the untilted and tilted image stacks with FREALIGN using the same procedure described above for untilted data. We analyzed pairs of images from tilted specimens in two different ways.

(1) Phase residual maps for all possible tilt axes. The application of a tilt transformation $\{rot_x, rot_y\}$ to the orientation determined for an untilted particle gives a predicted orientation for the tilted particles. The tilt transformation $\{rot_x, rot_y\}$ is a rotation by an angle of magnitude tiltangle $= \sqrt{rot_x^2 + rot_y^2}$ about an axis lying in the film plane in an orientation described by an angle tiltaxis $=$ arc tan(rot_y/rot_x). This transformation may be written as the Eulerian rotation ($\psi =$ tiltaxis, $\theta =$ tiltangle, $\phi = -$ tiltaxis) (program ANGPLOT). The agreement between the projection of the model in the predicted orientation with the tilted particle image was scored by the phase residual after refining the translation parameters (x, y) using data from 100–35 Å. Tilt transformations in 1° increments of both rot_x and rot_y, corresponding to all possible directions and tilt angles for the microscope goniometer, were applied to the untilted particle orientations. The average phase residual on the image of tilted particles was determined for 50–100 particles. The minimum phase residual in the resulting maps of $\{rot_x, rot_y\}$ identifies the calculated tilt angle and tilt axis direction. The procedure can be run automatically given tilted and untilted image stacks. The location and polarity of the laboratory axis on the micrograph must be identified as described above. Programs are provided as part of the MRC Image Processing Package.[38] These results are shown in Figures 3 and 5.

(2) Best tilt axis given untilted and tilted orientations. A tilt axis and angle were assigned to each particle pair (program TILTDIFF) using the Euler angles assigned separately to the untilted and tilted particles by searching for the minimum angular

error in transforming the untilted particle orientation onto the tilted particle orientation. The tilt axis was constrained to lie in the plane of the micrograph with a maximum tilt angle of 30°. The transformation was represented by an Eulerian rotation of the form ($\psi =$ tiltaxis, $\theta =$ tiltangle, $\phi = -$ tiltaxis). For a particle with symmetry, it is essential to test all symmetry-related orientations to find the tilt axis with minimum error. The result is shown in Figure 6.

Comparison to X-ray models

The X-ray models for *B. stearothermophilus* (PDB code 1b5s) or *A. vinlandii* (PDB code 1eea) E2CD were compared with the electron potential map density using the program O,[39] confirming the experimental assignment of absolute hand. Spherically averaged structure factors for the model (Figure 8) including solvent were computed using CRYSOL.[40] Additional structure factor calculations on maps were performed using programs from the CCP4 suite.[41] X-ray model structure factors were calculated with and without a flat bulk solvent model using XPLOR.[42] The magnification of the experimental map was decreased by 3% to match the X-ray model as determined by visual inspection and maximization of the correlation with the map calculated from the X-ray model.

Figures 2(c) and 9 were made using Surf.[43] Figure 10 was made using O.

References

1. Henderson, R. (1995). The potential and limitations of neutrons, electrons and X-rays for atomic resolution microscopy of unstained biological molecules. *Quart. Rev. Biophys.* **28**, 171–193.
2. van Heel, M. (1987). Angular reconstitution: a posteriori assignment of projection directions for 3D reconstruction. *Ultramicroscopy*, **21**, 111–124.
3. Sigworth, F. J. (1998). A maximum-likelihood approach to single-particle image refinement. *J. Struct. Biol.* **122**, 328–339.
4. Finch, J. T. & Klug, A. (1965). Structure of viruses of the papilloma-polyoma type III. Structure of rabbit papilloma virus with an appendix on the topography of contrast in negative-staining for electron-microscopy. *J. Mol. Biol.* **13**, 1–12.
5. Finch, J. T. & Klug, A. (1966). Arrangement of protein

subunits and the distribution of nucleic acid in turnip yellow mosaic virus II. Electron microscopic studies. *J. Mol. Biol.* **15**, 344–364.

6. Finch, J. T. (1972). The hand of the helix of tobacco mosaic virus. *J. Mol. Biol.* **66**, 291–294.

7. Klug, A. & Finch, J. T. (1968). Structure of viruses of the papilloma-polyoma type IV. Analysis of tilting experiments in the electron microscope. *J. Mol. Biol.* **31**, 1–12.

8. Belnap, D. M., Olson, N. H. & Baker, T. S. (1997). A method for establishing the handedness of biological macromolecules. *J. Struct. Biol.* **120**, 44–51.

9. Guinier, A. & Fournet, G. (1955). *Small-angle Scattering of X-rays*, Wiley, New York.

10. Wilson, A. J. C. (1942). Determination of absolute from relative X-ray intensity data. *Nature*, **150**, 152.

11. Frank, J. (1996). *Three-dimensional Electron Microscopy of Macromolecular Assemblies*, Academic Press, New York.

12. Hegerl, R. & Hoppe, W. (1976). Influence of electron noise on three-dimensional image reconstruction. *Z. Naturforsch*, **31a**, 1717–1721.

13. Grimm, R., Singh, H., Rachel, R., Typke, D., Zillig, W. & Baumeister, W. (1998). Electron tomography of ice-embedded prokaryotic cells. *Biophys. J.* **74**, 1031–1042.

14. Henderson, R. (1992). Image contrast in high-resolution electron microscopy of biological macromolecules: TMV in ice. *Ultramicroscopy*, **46**, 1–18.

15. Havelka, W. A., Henderson, R. & Oesterhelt, D. (1995). Three-dimensional structure of halorhodopsin at 7 Å resolution. *J. Mol. Biol.* **247**, 726–738.

16. Saxton, W. O. & Baumeister, W. (1982). The correlation averaging of a regularly arranged bacterial cell envelope protein. *J. Microsc.* **127**, 127–138.

17. van Heel, M. & Stoffler-Meilicke, M. (1985). Characteristic views of *E. coli* and *B. stearothermophilus* 30 S ribosomal subunits in the electron microscope. *EMBO J.* **4**, 2389–2395.

18. Blow, D. M. & Crick, F. H. C. (1959). The treatment of errors in the isomorphous replacement method. *Acta Crystallog.* **12**, 794–802.

19. Perham, R. N. (2000). Swinging arms and swinging domains in multifunctional enzymes: catalytic machines for multistep reactions. *Annu. Rev. Biochem.* **69**, 961–1004.

20. Izard, T., Aevarsson, A., Allen, M. D., Westphal, A. H., Perham, R. N., de Kok, A. & Hol, W. G. (1999). Principles of quasi-equivalence and Euclidean geometry govern the assembly of cubic and dodecahedral cores of pyruvate dehydrogenase complexes. *Proc. Natl Acad. Sci. USA*, **96**, 1240–1245.

21. Milne, J. L., Shi, D., Rosenthal, P. B., Sunshine, J. S., Domingo, G. J., Wu, X. *et al.* (2002). Molecular architecture and mechanism of an icosahedral pyruvate dehydrogenase complex: a multifunctional catalytic machine. *EMBO J.* **21**, 5587–5598.

22. Brink, J., Sherman, M. B., Berriman, J. & Chiu, W. (1998). Evaluation of charging on macromolecules in electron cryomicroscopy. *Ultramicroscopy*, **72**, 41–52.

23. Grigorieff, N. (1998). Three-dimensional structure of bovine NADH:ubiquinone oxidoreductase (complex I) at 22 Å in ice. *J. Mol. Biol.* **277**, 1033–1046.

24. Spence, J. C. H. (1988). *Experimental High-resolution Electron Microscopy*, Oxford University Press, New York.

25. Mattevi, A., Obmolova, G., Schulze, E., Kalk, K. H., Westphal, A. H., de Kok, A. & Hol, W. G. (1992). Atomic structure of the cubic core of the pyruvate

dehydrogenase multienzyme complex. *Science*, **255**, 1544–1550.

26. Mattevi, A., Obmolova, G., Kalk, K. H., Westphal, A. H., de Kok, A. & Hol, W. G. (1993). Refined crystal structure of the catalytic domain of dihydrolipoyl transacetylase (E2p) from *Azotobacter vinelandii* at 2.6 Å resolution. *J. Mol. Biol.* **230**, 1183–1199.

27. Jensen, G. J. (2001). Alignment error envelopes for single particle analysis. *J. Struct. Biol.* **133**, 143–155.

28. Thuman-Commike, P. A., Tsuruta, H., Greene, B., Prevelige, P. E., Jr, King, J. & Chiu, W. (1999). Solution X-ray scattering-based estimation of electron cryomicroscopy imaging parameters for reconstruction of virus particles. *Biophys. J.* **76**, 2249–2261.

29. Saad, A., Ludtke, S. J., Jakana, J., Rixon, F. J., Tsuruta, H. & Chiu, W. (2001). Fourier amplitude decay of electron cryomicroscopic images of single particles and effects on structure determination. *J. Struct. Biol.* **133**, 32–42.

30. Glaeser, R. M. (1999). Review: electron crystallography: present excitement, a nod to the past, anticipating the future. *J. Struct. Biol.* **128**, 3–14.

31. Reimer, L. (1997). *Transmission Electron Microscopy: Physics of Image Formation and Microanalysis*, Springer, Berlin.

32. Böttcher, B., Wynne, S. A. & Crowther, R. A. (1997). Determination of the fold of the core protein of hepatitis B virus by electron cryomicroscopy. *Nature*, **386**, 88–91.

33. Zhou, Z. H., Dougherty, M., Jakana, J., He, J., Rixon, F. J. & Chiu, W. (2000). Seeing the herpesvirus capsid at 8.5 Å. *Science*, **288**, 877–880.

34. Zhou, Z. H., Liao, W., Cheng, R. H., Lawson, J. E., McCarthy, D. B., Reed, L. J. & Stoops, J. K. (2001). Direct evidence for the size and conformational variability of the pyruvate dehydrogenase complex revealed by three-dimensional electron microscopy. The "breathing" core and its functional relationship to protein dynamics. *J. Biol. Chem.* **276**, 21704–21713.

35. Allen, M. D. & Perham, R. N. (1997). The catalytic domain of dihydrolipoyl acetyltransferase from the pyruvate dehydrogenase multienzyme complex of *Bacillus stearothermophilus*. Expression, purification and reversible denaturation. *FEBS Letters*, **413**, 339–343.

36. Harris, J. W. (1962). Holey films for electron microscopy. *Nature*, **196**, 499–500.

37. Jeng, T. W., Talmon, Y. & Chiu, W. (1988). Containment system for the preparation of vitrified-hydrated virus specimens. *J. Electron Microsc. Tech.* **8**, 343–348.

38. Crowther, R. A., Henderson, R. & Smith, J. M. (1996). MRC image processing programs. *J. Struct. Biol.* **116**, 9–16.

39. Jones, T. A., Zou, J. Y., Cowan, S. W. & Kjeldgaard, M. (1991). Improved methods for building protein models in electron density maps and the location of errors in these models. *Acta Crystallog. sect. A*, **47**, 110–119.

40. Svergun, D., Barberato, C. & Koch, M. H. J. (1995). CRYSOL—a program to evaluate X-ray solution scattering of biological macromolecules from atomic coordinates. *J. Appl. Crystallog.* **28**, 768–773.

41. Collaborative Computational Project, No. 4 (1994). The CCP4 suite: programs for protein crystallography. *Acta Crystallog. sect. D*, **50**, 760–763.

42. Brunger, A. T. (1992). *X-PLOR Version 3.1 Manual*, Yale University, New Haven, CT.

43. Vigers, G. P. A. (1986). *Clathrin Assemblies in Vitreous Ice: A Structural Analysis by Image Reconstruction*, Cambridge University, Cambridge, UK.

Appendix

An Objective Criterion for Resolution Assessment in Single-particle Electron Microscopy

The resolution of a three-dimensional density map calculated from single-particle images can be estimated by the Fourier shell correlation (FSC) between two independent maps, where each map is calculated from half the data.[A1,A2] However, disagreement exists as to what threshold value of the FSC, a function of resolution, should be used to define the limiting resolution of the map. Here, we propose a threshold criterion based on the estimated correlation between a density map calculated from a full set of image data and a perfect reference map, and identify the corresponding threshold for the FSC between maps calculated from data half-sets. This threshold criterion for single-particle electron microscopy is the same as a common measure of map interpretability in X-ray crystallography and provides a unified criterion for assessing the resolution of a structure determined by either technique.

The Fourier shell correlation is the complex correlation of structure factors (F_1,F_2) of two maps calculated from the data half-sets as follows:

$$\text{FSC} = \frac{\sum F_1 F_2^*}{\sqrt{\sum |F_1|^2 \sum |F_2|^2}} \qquad \text{(A1)}$$

where the sum runs over a resolution shell of reciprocal space voxels. The FSC includes both amplitude and phase information and its advantages over other resolution criteria have been discussed.[A3] Because the correlation over all of reciprocal space will be dominated by low-resolution terms, calculating the FSC in reciprocal space shells provides a more sensitive measure of its fall-off with resolution. When the value of the FSC curve is near 1.0, then the information contained in each reciprocal space voxel, on average, is a nearly perfect determination of the structure factor and has little noise.

Ideally, the FSC should be examined as a function of resolution to identify regions of reciprocal space with poor correlation, such as those due to zeroes of the CTF. However, identifying a single-value resolution for the map where the FSC drops below a threshold provides a rapid measure of map improvement during refinement and a common standard for reporting progress in the literature in the same way that common measures of structure quality are reported in X-ray crystallography. Such a standard resolution criterion should reflect the interpretability of a map in terms of molecular features but should not be dependent on irrelevant details of map calculation.

One commonly proposed threshold for identifying the resolution from the fall-off of the FSC is to observe where the FSC reaches the level expected from the FSC calculated for pure noise with a Gaussian distribution. This FSC for pure noise is given by $1/\sqrt{N}$, where N represents the number of voxels in a resolution shell, and the threshold is taken as either two or three times this figure. Such a threshold can be used as a relative measure of resolution for maps calculated in an identical way. Because it depends on the number of voxels in an arbitrary resolution shell of the map, it cannot provide an absolute resolution criterion. Suppose the structure of a molecule is determined both alone and in the context of a larger structure such that both maps are equally interpretable. Each reciprocal space voxel will have the same signal-to-noise ratio so that the plot of the FSC against resolution will be virtually identical. However, since the number of voxels between resolution shells will be different, the resolution assessment will be different because the noise correlation figure depends on the number of voxels. It has also been suggested that the noise figure for a symmetric structure should be $(1/\sqrt{N})\sqrt{N_{AU}}$, where N_{AU} is the number of asymmetic units, because symmetry-related pixels are not independent.[A4] However, a map with or without symmetry will be equally interpretable when the FSC is the same. Any threshold criterion that depends on the number of pixels in the map is not an absolute criterion for the evaluation of resolution.

Another common threshold criterion is to nominate the point where the FSC between data half-sets equals 0.5 as the resolution. This is an absolute criterion with a signal-to-noise ratio substantially greater than zero,[A5] and is not dependent on how the map is calculated. The arguments below suggest that it is an underestimate of the resolution, and that a better value for the threshold can be proposed, related to the interpretability of the map.

Individual structure factors for each half dataset can be represented by a common signal term with a noise term added, $F1 = S + N1$ and $F2 = S + N2$, and their correlation by:

$$C = \frac{\sum (S+N1)(S+N2)^*}{\sqrt{\sum |S+N1|^2 \sum |S+N2|^2}} \qquad \text{(A2)}$$

Assuming signal and noise are uncorrelated, and for data on the same scale, the above expression may be written as follows:

$$\text{FSC} = \frac{\sum |S|^2}{\sum |S^2 + N^2|} \qquad \text{(A3)}$$

When the correlation FSC is 0.5, $\langle S^2 \rangle$ is approximately equal to $\langle N^2 \rangle$ and half the power (F^2) in each data half-set is signal (S^2) and half is noise (N^2).

The threshold FSC = 0.5 is an underestimate of the resolution of the structure, because it describes the resolution of a map calculated from only half the data, and a map computed from more images will be of higher resolution. By definition there are never two independent full datasets to compare,

but the resolution of the full dataset can be estimated from the FSC as follows.

When the two halves of the data are averaged to produce the best estimate of the structure, the signal-to-noise ratio for the full average is increased by $\sqrt{2}$ relative to the half-set average, or equivalently, the noise term $N \to N/\sqrt{2}$ in expression (A3) and the FSC_{full} becomes:

$$\text{FSC}_{\text{full}} = \frac{\sum |S|^2}{\sum \left| S^2 + \frac{N^2}{2} \right|} = \frac{2\text{FSC}}{1 + \text{FSC}} \quad \text{(A4)}$$

By substituting (A3), the FSC, into the left part of (A4), the resolution estimate for a map computed from all the data can be written in terms of the FSC between maps calculated from half the data.[A6] When half the power is signal and half is noise, the FSC is 0.5 but the FSC_{full} is higher at 2/3 or 0.67. If we choose as the threshold $\text{FSC}_{\text{full}} = 0.5$, this occurs when the FSC is 0.33.

The choice of $\text{FSC}_{\text{full}} = 0.5$ is still too pessimistic. Ideally we desire a measure of the agreement between the best map we can calculate from a full dataset and a perfect map containing no errors. Though a perfect map is unknown, we can estimate the correlation from signal-to-noise arguments. Such a correlation can be obtained from expression (A2) by setting the noise term $N2 = 0$ in expression (A2) so that $F2 = S$ represents a perfect map without noise, setting $N1 = N/\sqrt{2}$ for the noise in a full dataset, and again assuming signal and noise are uncorrelated.

$$C_{\text{ref}} = \frac{\sum \left(S + \frac{N}{\sqrt{2}} \right) S^*}{\sqrt{\sum \left| S + \frac{N}{\sqrt{2}} \right|^2 \sum |S|^2}} = \sqrt{\frac{S^2}{S^2 + \frac{N^2}{2}}}$$

$$= \sqrt{\frac{2\text{FSC}}{1 + \text{FSC}}} \quad \text{(A5)}$$

In this case, when $\langle S^2 \rangle$ equals $\langle N^2 \rangle$, $C_{\text{ref}} = 0.816$. Again, substitution of FSC (A3) into the left-hand side of (A5) gives an expression for the correlation of the full dataset against a perfect reference in terms of the FSC. If we choose a threshold for C_{ref} of 0.5, this corresponds to an FSC of 0.143.

The choice of $C_{\text{ref}} = 0.5$ as a threshold can be justified for two reasons. First, we can write an expression for the correlation between a full dataset and a perfect reference which is equivalent to (A5) but in terms of structure factors as follows:

$$C_{\text{ref}} = \frac{\sum F_1 F_{\text{ref}}}{\sqrt{\sum |F_1|^2 \sum |F_{\text{ref}}|^2}} = \frac{\sum |F_1||F_{\text{ref}}|\cos(\Delta\phi)}{\sqrt{\sum |F_1|^2 \sum |F_{\text{ref}}|^2}} \quad \text{(A6)}$$

Here, the known structure factor of the perfect reference provides a perfect phase and the correlation with the experimental map is written in terms of $\Delta\phi$, the phase error. Expression (A6) is therefore the amplitude weighted average of cos

($\Delta\phi$) which is equivalent to the figure-of-merit m used in X-ray crystallography.[A7] A map with an average $m = 0.5$, corresponding to a phase error of 60°, is commonly regarded as interpretable, i.e. a molecular structure can be built.[A8] C_{ref} is therefore equivalent to a figure-of-merit, and an identical threshold may be adopted.

Second, the FSC is also related to the real space correlation coefficient, R, a common measure for the agreement of two density maps:

$$R = \frac{\langle \rho_1 \rho_2 \rangle - \langle \rho_1 \rangle \langle \rho_2 \rangle}{\sqrt{\langle \rho_1^2 \rangle - \langle \rho_1 \rangle^2} \sqrt{\langle \rho_2^2 \rangle - \langle \rho_2 \rangle^2}} \quad \text{(A7)}$$

When the map density is expressed as structure factors, $\langle \rho \rangle = (1/V)F(0)$, $\langle \rho^2 \rangle = (1/V^2)\sum |F^2|$, and $\langle \rho_1 \rho_2 \rangle = (1/V^2)\sum F_1(h)F_2(\bar{h})$. When an experimental map ρ_{exp} is compared with a perfect reference ρ_{ref}, and assuming no amplitude errors in the experimental structure factors, $\langle \rho_{\text{exp}} \rho_{\text{ref}} \rangle = (1/V^2)\sum |F_{\text{ref}}|^2 \cos(\Delta\phi)$. Then for maps on the same scale ($F(0) = 0$), the real space correlation coefficient R is identical with equation (A6):

$$R = \frac{\langle \rho_{\text{exp}} \rho_{\text{ref}} \rangle - \langle \rho_{\text{exp}} \rangle \langle \rho_{\text{ref}} \rangle}{\sqrt{\langle \rho_{\text{exp}}^2 \rangle - \langle \rho_{\text{exp}} \rangle^2} \sqrt{\langle \rho_{\text{ref}}^2 \rangle - \langle \rho_{\text{ref}} \rangle^2}}$$

$$= \frac{\sum |F_{\text{ref}}|^2 \cos(\Delta\phi)}{\sum |F_{\text{ref}}|^2} \quad \text{(A8)}$$

where the summation runs over all of reciprocal space.[A8] It has been shown that a sufficient condition for including an additional resolution shell that will improve the overall map correlation coefficient is that the additional resolution shell have a correlation of 0.5 against the perfect reference.[A8] However, if the amplitudes of the extra resolution shell are adequately large, a resolution shell with a lower correlation coefficient can still improve the map.

Therefore, choosing C_{ref} equal to 0.5 represents a single objective threshold criterion for the FSC independent of the way the maps are calculated. It is equivalent to a common measure of map interpretability for X-ray crystallography, the figure-of-merit, and identifies the highest resolution shell that is guaranteed to improve the map quality. In practice, a perfect reference map is unavailable, but a C_{ref} of 0.5 is equivalent to an FSC of 0.143 between data half-sets.

Table A1 below shows corresponding values for a given map quality for each of the correlation coefficients outlined above. The proposed threshold criterion unifies common measures of

Table A1. Correlation coefficients

FSC	FSC_{full}	C_{ref}	Phase error (deg.)	$S/N_{1/2}$	S/N_{FULL}
0.50	0.67	0.82	35	1.00	1.41
0.33	0.50	0.71	45	0.71	1.00
0.14	0.25	0.50	60	0.41	0.58

map quality used in both single particle microscopy and crystallography, including the Fourier shell correlation, the figure-of-merit, and the real space correlation coefficient.

Assignment of an appropriate weight to a structure factor based on its probability of being the true structure factor should improve the map calculation as with a figure-of-merit. C_{ref} is a measure of the average signal-to-noise ratio in a given reciprocal space resolution shell and the error in the structure factors. Noise-weighted structure factors can be calculated as $C_{ref}F$ where $C_{ref} = \sqrt{(2FSC)/(1 + FSC)}$ for the resolution shell. C_{ref} will have a value near 1.0 in well-determined shells, but will decrease at high resolution where the structure is less certain. In the main text we apply this weighting scheme to maps to determine more accurately the fall-off of structure factor amplitudes with resolution and to suppress noise when applying a positive temperature factor during map sharpening.

Acknowledgements

References

A1. Saxton, W. O. & Baumeister, W. (1982). The correlation averaging of a regularly arranged bacterial cell envelope protein. *J. Microsc.* **127**, 127–138.

A2. van Heel, M. & Stoffler-Meilicke, M. (1985). Characteristic views of *E. coli* and *B. stearothermophilus* 30 S ribosomal subunits in the electron microscope. *EMBO J.* **4**, 2389–2395.

A3. van Heel, M. (1987). Similarity measures between images. *Ultramicroscopy*, **21**, 95–100.

A4. Orlova, E. V., Dube, P., Harris, J. R., Beckman, E., Zemlin, F., Markl, J., van Heel, M. *et al.* (1997). Structure of keyhole limpet hemocyanin type 1 (KLH1) at 15 Å resolution by electron cryomicroscopy and angular reconstitution. *J. Mol. Biol.* **271**, 417–437.

A5. Penczek, P. (1998). Appendix: measures of resolution using Fourier shell correlation. *J. Mol. Biol.* **280**, 115–116.

A6. Grigorieff, N. (2000). Resolution measurement in structures derived from single particles. *Acta Crystallog. sect. D*, **56**, 1270–1277.

A7. Blow, D. M. & Crick, F. H. C. (1959). The treatment of errors in the isomorphous replacement method. *Acta Crystallog.* **12**, 794–802.

A8. Lunin, V. Y. & Woolfson, M. M. (1993). Phase error and the map correlation coefficient. *Acta Crystallog. sect. D*, **49**, 530–533.